Hyperpolarised Xenon MRI and Time-resolved X-ray Computed Tomography Studies of Structure-Transport Relationships in Hierarchical Porous Media

Fraser Hill-Casey[a,b], Thomas Hotchkiss[c], Katherine A. Hardstone[d], Iain Hitchcock[d], Vladimir Novak[e], Christian M. Schlepütz[e], Thomas Meersmann[b,f], Galina E. Pavlovskaya[b], Sean P. Rigby[a,*],

[a]Department of Chemical and Environmental Engineering, University of Nottingham, NG7 2RD, UK.

[b]Sir Peter Mansfield Imaging Centre, School of Medicine, University of Nottingham, NG7 2RD, UK

[c]Johnson Matthey, 2A Orchard Rd, Royston, SG8 5HE, UK

[d]Johnson Matthey Technology Centre, Blount's Court, Sonning Common, Reading, RG4 9NH, UK

[e]Swiss Light Source, Forschungsstrasse 111, CH-5232 Villigen PSI, Switzerland

[f]Faculty of Science and Engineering, University of Nottingham Ningbo China, 199 Taikang East RD, Ningbo 315100, China

Abstract

Catalysed diesel particulate filter (DPF) monoliths are hierarchical porous solids, as demonstrated by mercury porosimetry. Establishing structure-transport relationships, including assessing the general accessibility of the catalyst, is challenging, and, thus, a comprehensive approach is necessary. Contributions, from each porosity level, to transport have been established using hyperpolarised (hp) xenon-129 magnetic resonance imaging (MRI) of gas dispersion within DPF monoliths at variable water saturation, since X-ray Computerised-Tomography, and ^{1}H and ^{2}H NMR methods, have shown that porosity levels dry out progressively. At high saturation, hp ^{129}Xe MRI showed gas transport between the channels of the monolith is predominantly taking place at channel wall intersections with high macroporosity. The walls themselves make a relatively small contribution to through transport due to the distribution of the micro-/meso-porous washcoat layer away from intersections. Only at low saturation, when the smallest pores are opened, do hp ^{129}Xe MR images became strongly affected by relaxation. This observation indicates accessibility of paramagnetic (catalytic) centres for gases arises only once the smallest pores are open.

Keywords: hyperpolarised xenon MRI: NMR relaxation; CT; diffusion; flow; catalyst; SCR monolith; filter; pore network

1. INTRODUCTION

Recently, hierarchical porous solids have become of particular interest for various applications, such as supercapacitors, PEM fuel cells, tissue engineering scaffolds, drug delivery devices, and heterogeneous catalysts [1–6]. One particular class of hierarchical porous solid is the catalysed diesel particulate filter (DPF) which reduces gas pollutant emissions from vehicle exhausts by selective catalytic reduction (SCR) and also filters out particulates. Catalysed DPFs typically consist of a catalytically-active washcoat applied to an inert monolithic support. The monolith comprises macroscopic-scale channels with macroporous walls. The washcoat typically comprises microporous zeolite crystallites and a mesoporous alumina binder. Hence, the catalysed DPF is a hierarchical system with void spaces on four different levels.

Different hierarchical materials, and different levels in the porosity hierarchy within the same material, can possess differing levels of order, depending upon the synthesis method(s) of the materials. With catalysed DPFs the catalyst is applied as a washcoat, and then the system is dried. Both the application and drying process may result in a heterogeneous distribution of washcoat within the amorphous macroporous wall structure of the monolith. Further, the amorphous nature of the washcoat binder means disorder at the mesoporous length-scale. Hence, the catalysed DPF system consists of a mixture of ordered (macroscopic channels and zeolite micropores) and disordered (washcoat distribution and binder mesopore network) structures.

The underlying structure of a hierarchical material affects its performance in application, often through the impact that structure has on mass transfer rates in the material. In operation of a catalysed DPF exhaust gas from the engine enters the inlet channels. Due to the impermeable plugs at the opposite end of these channels, the gas flow is forced to pass through the

macroporous (and therefore permeable) walls, separating the macroscopic channels, where the meso-/micro-porous washcoat is located. The porous wall acts like a filter such that the particulates in the exhaust gas are deposited within the inlet channel, and potential gaseous pollutants are reacted away as the gas stream passes over the catalyst within the washcoat, allowing for clean gas to emerge from the outlet channels. However, for the catalytic clean-up of the exhaust gases to happen the gas stream must be routed through the pores containing the catalyst. The heterogeneity and disorder present in the washcoat spatial distribution and mesopore network architecture provide opportunities for both bypassing of the catalyst and creating resistance to flow, which would reduce overall performance in reducing emissions [7]. Hence, it is critical to know how the individual levels in the hierarchical structure of the catalysed DPF affect mass transport. Previous work [8] has used mercury entrapped, following intrusion to different pressures, to progressively block off different ranges of pore sizes within a macro/meso-porous catalyst pellet, and then their relative importance to mass transport was assessed via comparisons of the uptake of nitrogen gas before and after their loss. However, in order to prevent contamination with mercury vapour it must be frozen in place (mpt -38.8 ºC), and thus the method is unsuitable for studying structure-transport relationships at other conditions. Further, only the spatial distribution of the blocked pores was obtained (by X-ray computed tomography (CT) of the mercury) and not the spatial variation in mass transport rates.

Mass transport processes within catalysed DPFs, in particular, have been studied both by computer simulation and empirical means. The issue with the simulation is that it is necessary to understand the key aspects of the structure of the catalysed DPF that need to be incorporated into the computer model before the model delivers information on the flow, but that information on the flow will be inaccurate if the representation of the structure is too much in error or incomplete. The empirical methods that can deliver the most detailed information on

(structure and) mass transport are the imaging methods. Magnetic resonance imaging (MRI) methods have been used to study mass transport in monoliths and catalysed DPFs. Earlier studies [9]–[11] have obtained velocity-weighted images of flows in alumina monoliths with different channel geometries and have looked at the flow of thermally-polarised hydrocarbon gases (ethyne, butane and propane). Previous workers [12] studied drying processes in monoliths and liquid flow velocity in monolith channels using MRI. However, catalysed DPFs operate with the fluid flow largely in gas phase, and thus previous work [13] studied the flow of gaseous SF_6 within monolith channels, and considered the uniformity of permeation of the gas into the walls along the channel. In order to obtain sufficient NMR signal to image the gaseous SF_6 the system had to be operated at high pressure so the gas density was high and this meant the pore diffusion mechanism was molecular. In contrast, the real system operates under conditions (temperature range 150-400 °C, but typically 300 °C, and 1 atm) such that the gas density is much lower and diffusion can occur by the different Knudsen mechanism, which has much greater sensitivity to pore structure since the Knudsen diffusivity is proportional to pore size, while molecular diffusivity is not [14]. Further, the transport of the gas through the walls was only studied in an indirect way.

The high NMR signal intensity associated with hyperpolarized (hp) noble gases [15], [16] enables MRI of the gas phase at conditions of the low density Knudson regime [17]. The hyperpolarized spin state survives brief passage through a high temperature reactions zone, thus enabling in-situ hp ^{129}Xe NMR spectroscopy [18] and in situ hp ^{129}Xe MRI [19] of a combustion process that is unfathomable through conventional, thermally polarized magnetic resonance methods [20]. Furthermore, the chemical shift of ^{129}Xe in a porous medium is strongly temperature dependent; an effect that has been used as a probe of the start-up phase of a hydrogenation reaction [21]. Pulsed field gradients (PFGs), commonly utilised to achieve spatial encoding in MRI, can also be used to extract temporally-resolved low pressure gas

transport data on the migration of gases in porous materials using hp noble gas NMR spectroscopy [22]–[24] and MRI [17], [25]–[27]. Alternatively, remote-detection or time-of-flight MRI methods can be employed to explore gas flow within porous media such as silica aerogel [28] or for the characterisation of micro-fluidic reactors [29]. The latter study used para-hydrogen induced polarization instead of hp noble gases that allows monitoring of reactions. Hp ^{129}Xe time of flight dispersion can be used to MR image spatial heterogeneity [28]. In particular, the methodology provides insights into reactors that cannot be detected directly, such as if it takes place within the confinement of a conducting container material that does not allow for radiofrequency signals to penetrate.

However, the remote detection methodology does not allow for a directly detected dimension (i.e. frequency encoding of one of the spatial dimensions) and therefore may lead to prolonged experimental times, although this effect may be offset by more efficient detection methods using small radiofrequency coils [30]. In this work, the mass transport properties of each region of the sample will be measured directly to avoid such complications.

It is the purpose of this work to utilise hp ^{129}Xe techniques to directly study gas phase mass transport at low pressure more akin to actual working conditions of catalysed DPF operation, which involve Knudsen regime pore diffusion. The other key aim is to assess the relative importance of different levels of the pore size hierarchy, and of structural heterogeneity, to mass transport. The relationship between structure and mass transport will be studied by progressively *opening-up* different levels in the pore size hierarchy for mass transport by progressive drying of an initially fully-saturated sample. Time-resolved X-ray computed tomography (CT) and ^{1}H, ^{2}H, and hp ^{129}Xe NMR relaxation measurements will be used to demonstrate that the drying process in the DPF occurs in a hierarchical fashion, with progressively smaller pores drying out with decreasing liquid saturation. MRI methods will also be used to obtain information on the spatial distribution of locally-averaged porosity and

pore size. The findings from the NMR methods are further validated using mercury porosimetry. The hp xenon NMR experiments will also be used to probe the general accessibility of the catalytic centres. The paramagnetic nature of the catalyst means that, when xenon gas comes into contact with it, the xenon signal will rapidly decay. Hence, during the drying experiments, as progressively smaller pores are opened up, the rapid decay of the xenon gas signal reveals just when the xenon can directly access the catalyst. This will reveal for which sets of transport pores some catalyst is available to the gas. Finally, the obtained knowledge concerning pore hierarchy, pore accessibility, and relaxation will be utilized to interpret the obtained MRI contrast based on xenon diffusional permeation under flow conditions at variable saturation levels.

2. EXPERIMENTAL

2.1 X-ray Computed Tomography

2.1.1 Monolith sample

X-ray tomography images were obtained of a section of the Combined SCR filtration monolith. Using a coring tool, an approximately 2 cm diameter, 7 cm length core was taken from the monolith. The cutting procedure generated dust so an air gun was used to remove any excess powdered sample from the monolith channels after cutting. The sample was placed in an XRADIA Versa XRM - 500 x-ray CT apparatus and images were acquired with a resolution of 2.99 μm/pixel.

2.1.2 Time-resolved tomographic imaging of drying

Time-resolved tomographic imaging was carried out at the TOMCAT beamline (Swiss Light Source). A monolith segment 12 mm in diameter and 20 mm in length was cored from an SCR filter. The sample was fixed into an aluminum holder mounted on a rotating stage, as shown in Figure 1. Prior to the drying experiment, the sample was filled with deionized water using a plastic pipette and the sample rotation was initiated at 180 degrees/s. Then two air heaters with diameter of 25 mm (LE MINI from Leister) set to a constant temperature of 55ºC were moved into position at opposite sides of the sample. The sample was thus heated simultaneously from both sides at the center of the monolith section.

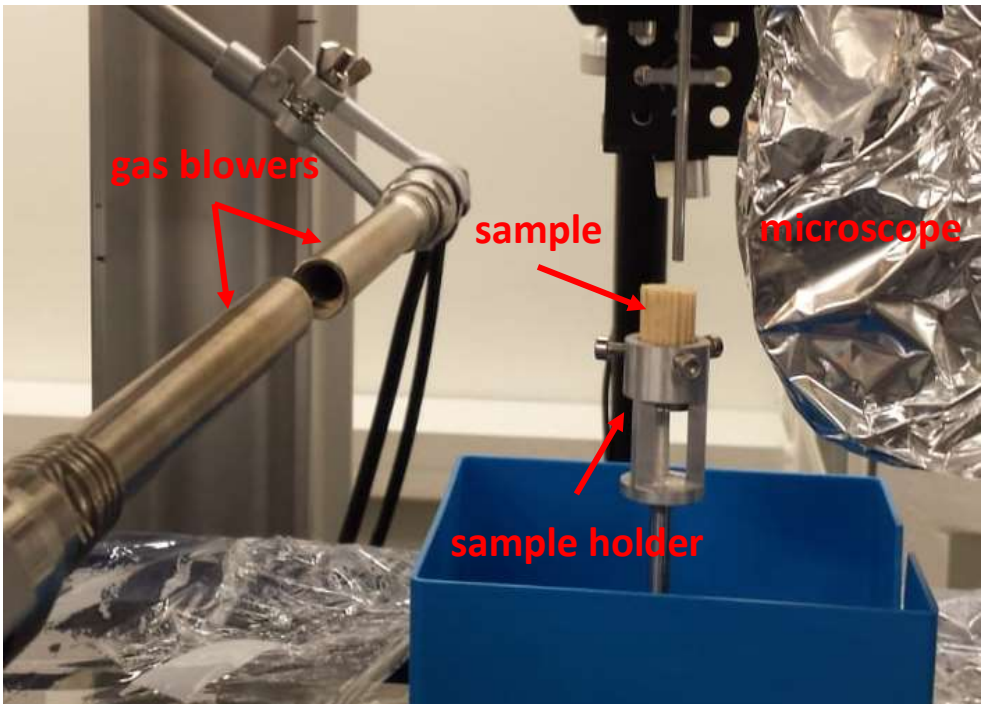

Figure 1. A picture of the experimental configuration at TOMCAT beamline including sample and sample holder, air heaters and microscope covered in aluminum foil to protect it from the heat. The setup for the drying was as shown in picture except that the gas blowers are moved to the right at the beginning of the drying (they were

moved away to left to provide for clarity of the sample position in the photo). This way the blowers are kept at the drying temperature, but they are kept away from the sample during the sample mounting and closing the hutch.

Filtered polychromatic X-ray radiation with a peak energy of about 26 keV originating from a 2.9 T bending magnet source was used for all experiments. An in-house developed GigaFRoST camera [31] and a high-resolution white-beam microscope (Optique Peter) with 13.7× magnification were used, yielding an effective pixel size of 0.8 μm. To capture the full extent of at least one or even several channels, an extended field-of-view scanning procedure was used where the rotation axis of the sample is aligned with one side of the detector's field-of-view and the sample is rotated through 360 degrees instead of the 180 degrees normally required for the parallel beam geometry [32]. The resulting field of view was 3950×1990 pixels, meaning that size of the scanned section was 3162×3162×1612 μm^3. The exposure time per projection was 1 millisecond with 2001 projections per 360 degrees scan. Consequently, the total time to acquire a single scan was 2 seconds, and subsequent scans were acquired every 10 seconds to reduce the amount of the collected time-series data. During the 8 seconds pause between two scans, a fast X-ray shutter was closed to prevent unnecessary sample exposure to the beam. In total, 101 scans were obtained capturing approximately 17 minutes of the drying process.

The 3-dimensional volume data sets were reconstructed using the propagation-based phase contrast method by Paganin *et. al* [33] and the gridrec algorithm [34]. The reconstructions were registered using Correct 3D Drift Fiji plugin [35] and subsequently processed in Fiji [36]. Two types of tomography images are discussed in the paper. The first type is a reconstructed image without post processing and thus it is referred to as "unprocessed". In such an image, the grey level values are related to the X-ray interaction strength of a material. The ceramic substrate

appears as the brightest shade, because it interacts more strongly with the X-ray beam, followed by Cu-zeolite coating in the ceramic substrate, water and the darkest air.

The second type of image aims to depict changes initiated by the movement of water-air interfaces. The images are constructed by subtracting an unprocessed image at time *t* from an unprocessed image at time 0 seconds (just after the sample was filled with water). Therefore, the images will be referred to as "subtracted". In such an image, the brightest shades correspond to a contrast change when water is removed. In contrast, the darkest shades show initially empty pores filled with water. The mid-grey levels code the starting state of the sample, which includes water, unfilled pores, ceramic substrate and Cu-zeolite coating. At the end of the drying, when all water is removed from the structure, only the solid phase (ceramic substrate and Cu-zeolite) remains in mid-grey shade as it does not change over time.

2.2 Mercury porosimetry

Since mercury does not wet most substances, it will not spontaneously penetrate pores by capillary action. Therefore, an external pressure is needed to force the mercury to enter the pore structure, with the equilibrium pressure required being inversely proportional to the size of the pores. The radius of the pores (r) may be determined from the following semi-empirical equation:

$$r = \frac{-A+\sqrt{A^2-2B\,P_{hg}}}{P_{hg}} \qquad (1)$$

where P_{hg} is the applied pressure, and A and B are constants dependent on the material. Eq. (1) is empirical in origin, and, thus, of limited scope, and, hence, is only applicable in a limited range of applications. Further, the size obtained from Eq. (1) contains experimental error of

approximately 4-5%. For further discussion on mercury porosimetry the reader is directed to previous work [37], [38].

2.3 Relaxometry

In order to non-destructively probe the pore structure of the SCR monolith, the spin-lattice (T_1) and spin-spin (T_2) relaxation of the NMR signal were utilised to probe adsorbed ganglia sizes. The value of T_2 or T_1 may be converted to a surface area to volume ratio (*S/V*) by the adoption of a relaxation model. For a liquid imbibed within a confined space, the relaxation rate decreases with decreasing *S/V* due to interactions, and reduced motion, within a thin surface-affected layer. Diffusional exchange between this interfacial layer and the remainder of the liquid (i.e. in the core of the pore) leads to an increased relaxation rate observed for the bulk liquid. For the systems studied in the this work, the liquid ganglia are several orders of magnitude smaller than the rms displacement of the probe water molecules during the course of the experiment, such that the ‘‘two-fraction fast exchange model’’ [39], [40] can be used to calculate the relaxation rate. The observed relaxation rate $1/T_{1,obs}$ is a weighted average of both contributions from the bulk liquid and pore surface:

$$\frac{1}{T_{1,obs}} = \frac{1-P_S}{T_{1,B}} + \frac{P_S}{T_{1,S}}, \tag{2}$$

where T_{1S} and T_{1B} refer to the relaxation in the surface layer and bulk fluid, respectively. $T_{1,obs}$ is the observed spin-lattice relaxation. P_s represents the proportion of spins absorbed in the surface layer and is described by:

$$P_S = \lambda \frac{S}{V} \quad , \tag{3}$$

where λ is the thickness of the surface-affected layer, and *S/V* is the surface area to volume ratio. Substitution of Eq.(3) into Eq.(2) gives:

$$\frac{1}{T_{1,obs}} = \left(1 - \lambda\frac{S}{V}\right)\frac{1}{T_{1,B}} + \left(\lambda\frac{S}{V}\right)\frac{1}{T_{1,S}} \quad . \tag{4}$$

In general $T_{1B} >> T_{1S}$ and thus S/V is given, approximately, by:

$$\frac{S}{V} = \frac{T_{1,S}}{\lambda}\,\frac{1}{T_1} \quad . \tag{5}$$

Equivalent expressions to Eqs.(4) and (5) can be obtained for spin-spin relaxation for small pore size limit. Further, for a completely saturated cylindrical pore, S/V would be equal to $2/r$, where r is the radius. Therefore, relaxation time is then proportional to the characteristic pore size.

Usually, T_2 measurements through CPMG protocols, provide a faster method to explore the pore sizes, compared to T_1 relaxation obtained through inversion recovery that requires point by point acquisition. However, the purpose of the ^{1}H and ^{2}H relaxation study is to generate supporting data for the exploration of the porous hierarchy through ^{129}Xe T_1 paramagnetic relaxation and its effect on hp ^{129}Xe MRI contrast. Unlike T_2 relaxation that is strongly affected by magnetic susceptibility effects at the gas to material interface, the ^{1}H T_1 relaxation in the monolith is predominantly caused by paramagnetic relaxation and, together with ^{2}H T_1 quadrupolar relaxation, provides complementary data for the interpretation of the ^{129}Xe T_1 relaxation, as discussed below.

2.4 NMR and MRI studies of drying and mass transport.

2.4.1. Sample preparation for drying experiments

Determination of T_1 at variable sample saturation for the two nuclei used in the studies was performed by initially drying the SCR monolith (see Figure 2) in a vacuum oven for 12 hours at 110 ºC using a vacuum of 20 Pa. The monolith segment was then saturated with either distilled water for ^{129}Xe (BOC gas, UK) and ^{1}H experiments, or deuterium oxide (sigma Aldrich, United Kingdom), for 15 minutes so as to ensure the pore structure was fully filled.

The monolith segment (diameter 14.4 mm, length 25 mm) was placed inside a custom-made acrylic container (i.d. 14.5 mm, length 25 mm) which was designed to minimise the empty volume. This consideration was specifically important to the ^{129}Xe studies, since any volume not filled by the monolith segment would lead to a pool of xenon with an extremely long relaxation time. This would allow for exchange between xenon in contact with the sample and the pool of *free* slow-relaxing xenon.

Variable saturation of the SCR monolith was achieved by applying a vacuum to the sample between relaxation experiments to remove the moisture from the sample. In order to determine the free pore volume, the sample was removed from the NMR magnet and weighed to determine the change in moisture content between relaxation experiments.

2.4.2. Sample preparation for MRI studies of mass transport.

As will be seen below in CXT images, the SCR monolith consists of 1.3 mm (wall to wall) diameter large channels and 1.0 mm diameter small channels. The wall thickness is about 330 μm and is identical to the thickness of the material across the corners. A segment of SCR

monolith (diameter 14.2 mm, length 65 mm) was dried for 12 hours in a vacuum oven at 110 ºC, and then saturated in distilled water for 15 minutes. After saturation, the sides and bottom of the monolith segment were wrapped in parafilm to ensure gas flow must leave only through the open channels. Gas was delivered to the central, dead-end channel by use of a 1/16' PFA tubing (Swagelok, Ohio U.S.A) modified to fit snugly within the channel. The modified PFA tube penetrated 6 mm into the monolith; as such, the sample assembly was positioned within the aforementioned 15 mm homebuilt ^{129}Xe coil so to ensure that the inlet tube would not interfere with measurement.

The drying of the SCR monolith, in this series of experiments, was performed, so as to conserve xenon between the experiments, by switching the gas flow to molecular nitrogen (N_2 5.0 grade) flowing at the same rate as that of the hp fuel mixture.

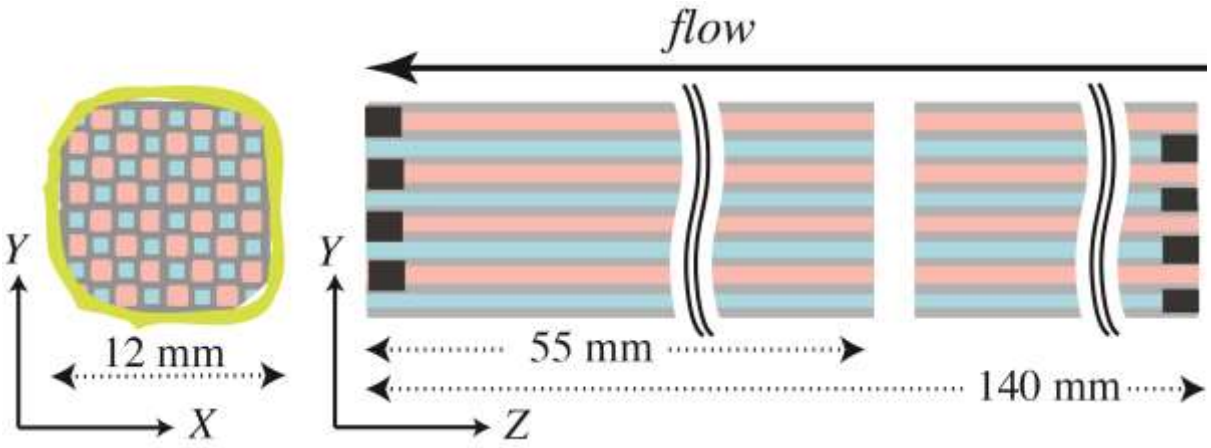

Figure 2. Schematic of the combined selective catalytic reduction monolith used in this work, illustrating a top-down view (a); and a longitudinal cross section (b) showing the location of the 55 mm section of the core as used in this work. It is depicted to be wrapped in Parafilm that is used to prevent gas leakage during the hp ^{129}Xe flow MRI experiments.

2.5 Experimental details of NMR spectroscopy and MRI.

NMR and MRI of all spin species reported in this study were performed on a 9.4 T Bruker Avance III Microimaging system (Bruker, Germany). Single-channel 25 mm commercial microimaging coils (Bruker, Germany) tuned to the resonance frequency of 400.18 MHz for protons and to 61.43 MHz for deuterons were used for all ^{1}H and ^{2}H experiments. The length of the ^{1}H $\pi/2$ pulse was 32 μs at 150 W, the dwell time was set to of 12.6 μs, and the resonance offset was set at the maximum of the proton peak height in each experiment or a series of consecutive experiments. The length of the ^{2}H $\pi/2$ hard pulse was 62 μs at 200 W, the dwell time was set to of 12.6 μs, and the resonance offset was set at the maximum of the deuterium peak height in each experiment or a series of consecutive experiments. A home-built 15 mm saddle coil tuned to the ^{129}Xe resonance frequency of 110.69 MHz was used in all ^{129}Xe experiments, the length of ^{129}Xe $\pi/2$ pulse was 62 μs at 150 W, the dwell time was set to 40 μs, and the resonance offset was set at the maximum of the gas phase xenon peak height in each experiment or a series of consecutive experiments. Specific experimental spectroscopic and imaging details are given below.

Proton and Deuterium T_1 relaxation was measured using the inversion recovery method [41] for both species. The data were acquired using 16 time delays, 4 scans for each time delay with recycle delays of 2 s and 1.165 s for proton and deuterium species, respectively.

Xenon-129 T_1 relaxation in the gas phase in the presence of the combined SCR monolith was measured using a home-written TopSpin3.2 pulse sequence consisting of sixty four 12^{o} flip angle pulses applied after each evenly spaced time delay τ with the signal recorded in the end of each time interval. The sequence was synchronised to the delivery of the hp gas to the NMR probe containing the SCR monolith prior detection to account for possible variations in the

delivery time. Therefore, the data recorded at time intervals after maximum integrated intensity were used in the analysis.

Axial deuterium spin-density images were acquired using a TopSpin3.2 slice-selective gradient echo sequence. In this context the axial image plane is defined as the plane whose normal is parallel to the long axis of the channels. The width of the slice-selective $\pi/2$ sinc-shaped pulse was 1.35ms, the recycle delay was 1s, the spectral width was 100 kHz. Images were collected into 128×128 matrices with the slice-selection gradient set to 2.5%, the phase encoding time of 0.665ms, and with maximum phase and read gradients set to 71.85% and 79.15%, respectively, resulting in a FOV of 12.8 ×13.6 mm^2 and the slice thickness of 16 mm. The images were reconstructed in Prospa 3.2 (Magritek, New Zealand) by zero filling to 256×256 matrices, sinc-squared apodisation performed in both dimensions with consecutive magnitude two-dimensional Fourier transformation. The resolution of processed images was approximately 0.05 mm^2 in the axial plane. The integrated image intensity was used to determine free pore volume in each image by normalizing the integrals obtained from each image to that corresponding to the complete saturation with D_2O, or at 0% free pore volume.

Deuterium T_2 contrast imaging in a fully saturated monolith was performed using a TopSpin 3.2 home written spin-echo imaging sequence with a rectangular $\pi/2$ excitation pulse of 60 μs and a gauss-shaped π pulse of 646 μs. The spectral width was set to 50 kHz, the recycle delay was 1s, and each image was collected with 16 scans to achieve sufficient signal to noise ratio for subsequent exponential analysis. The phase encoding gradient was set to 42% and the read gradient was set to 33% resulting in FOV=15.4 mm^2. The slice selection gradient was 0.25% resulting in 81 mm thick slice to ensure that the signal was collected from the entire monolith segment under investigation. Eight separate 256×128 images were acquired at 1.7, 7.7, 11.7, 16.7, 21.7, 26.7, 31.7 and 41.7 ms τ delays used for in-voxel exponential analysis to produce a

T_2 relaxation map of the fully saturated monolith. The images were then processed as described in the previous section. Subsequent T_2 mapping in the monolith segment were performed in Prospa3.02 (Magritek, New Zealand) using its built-in features. Histogram, and its deconvolution, analysis were performed with IgorPro 8.02 (Wavemetrics, USA) using its built-in functions.

HP ^{129}Xe imaging in spatial dispersion experiments was performed using a home written TopSpin3.2 two-dimensional gradient echo sequence with slice-selection. The width of the slice-selective $\pi/2$ sinc-shaped pulse was 0.5 ms, the recycle delay was 2 s, and the spectral width was 12.5 kHz. Axial images were collected into 64×32 matrices with slice-selection gradient set to 1%, phase encoding time of 1.29ms, and with maximum phase and read gradients set to 4% and 3.2%, respectively, resulting in axial FOV of 17.5×22 mm^2 and the slice thickness of 15.8 mm. The images were reconstructed in Prospa 3.2 (Magritek, New Zealand) by zero filling to 128×128 matrices, sinc-squared apodisation performed in both dimensions with consecutive magnitude two-dimensional Fourier transformation. The resolution of processed images was approximately 0.136×0.171 mm^2 in the axial plane.

Axial spin density images were acquired at a steady state flow of dry hp ^{129}Xe flowed through a single, closed end channel (see Figure 2) as described above at a flow rate of 250 mm^3/s at 21 ºC.

Since the MR active gas in question is hyperpolarised in nature, each $\pi/2$ pulse of the imaging sequence will fully destroy the magnetisation of the gas within the rf coil. Therefore, the dominant effect on signal replenishment is the rate at which the freshly polarised gas enters the detection region rather than the size of T_1. Thus, by altering the inter-pulse or recycle delay of the imaging sequence, we may investigate the process of dispersive mass transport across the monolith segment, as a longer inter-pulse delay would allow the gas to spread further

throughout the structure before destruction of the magnetisation than a shorter one. Further, as the monolith dried, and, thus, the free pore volume fraction increased, the hp gas may transverse new pathways within the pore structure, and also potentially interacted with the paramagnetic components within the wash coat in the pore structure.

2.6 Hyperpolarised ^{129}Xe gas production and delivery.

Hyperpolarised ^{129}Xe was produced though Spin Exchange Optical Pumping (SEOP) (see Figure 3) by a custom-built instrument described in detail elsewhere [15,16]. Two methods were used for hp ^{129}Xe production within this work, as will be described below.

First, for relaxation experiments, a 5 % Xe (natural isotopic abundance): 95 % N_2 SEOP fuel mixture was polarised in *batch mode*. The SEOP cell pressure was ~158 kPa and spin polarisation was allowed to build up over 6 mins before delivering the now hp gas to the evacuated sample by pressure equalisation resulting in a detection cell pressure of 115 kPa. The nuclear spin polarisation for the batch mode was approximately P = 48 % spin polarisation. However, since the hp ^{129}Xe was diluted with buffer gas from the SEOP process, a better measure of the expected signal intensity is the apparent polarization $P_{app} = P \times [\mathrm{Xe}]/[\mathrm{N_2}]$ that takes the dilution into account [15], [16]. For the mixture of 5 % Xe in 95 % N_2 that was used the P_{app} = 2.4 %.

Second, for the mass transport imaging measurements, hp ^{129}Xe was produced in continuous flow mode. The major difference with the first method is that the outlet of the SEOP cell is opened, and the inlet also remains open, thus providing a constant flow of gas which is polarised *in stream* [42]. The flow of gas in this mode was controlled using two needle valves, located before and after the sample. The spin polarisation in this mode was highly dependent on the time of flight that the ^{129}Xe remains in the SEOP apparatus. In the continuous flow mode

a 25 % Xe (natural abundance): 75 % N_2 mixture was used to provide a spin polarisation of ~ 3.2 %, and an apparent polarisation of ~ 0.8 %, from a cell residency time of ~ 5 seconds. A steady flow was allowed to develop before imaging experiments were begun.

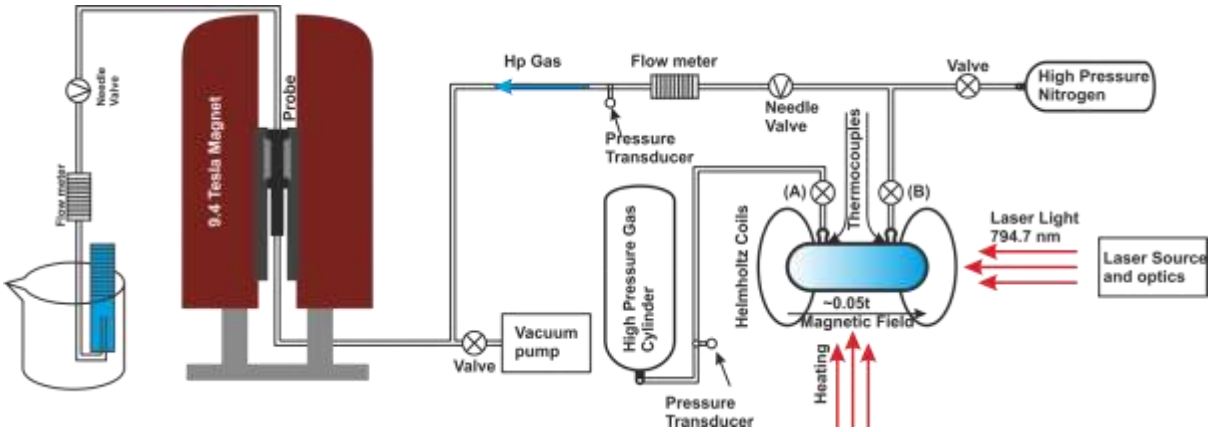

Figure 3. The experimental apparatus used for both **Batch Mode** and **Continuous flow** Spin Exchange Optical Pumping (SEOP); The delivery path of the hp gas to the high field magnet and major components of the experimental apparatus are outlined. **Batch Mode** gas is delivered to the SEOP cell, then valves (A) and (B) are closed, and the gas mixture is then allowed to polarize for 6 minutes before being *vacuum* shuttled to the sample container. In contrast, for **Continuous flow** SEOP, **t**he gas mixture was delivered to the cell and both valves (A) and (B) remained open, allowing the gas to flow from the high pressure cylinder though the SEOP cell and on to the sample. The pressure of the SEOP cell was controlled by use of a pressure regulator at the high pressure gas cylinder, while the needle valves allowed for fine adjustment of the flow rate through the sample container. High pressure nitrogen and a vacuum pump were used to control the drying of the sample.

2.7 NMR data analysis.

2.7.1 Analysis of Proton and Deuteron T_1 Relaxation.

The changes in the T_1 of the ^1H or ^2H nuclei within a monolith segment, saturated either in ordinary or heavy water, were monitored over the drying of the monolith segment by use of a standard T_1 inversion recovery sequence [41]. Data were collected using 16 inversion recovery delays, τ, and then fitted to a bi-exponential model for low free pore volumes:

$$I = A - 2 * A * e^{-\frac{\tau}{T_{1A}}} + B - 2 * B * e^{-\tau/T_{1B}} \quad (6)$$

where *A* and *B* each represent the signal intensity that is proportional to the amount of the nuclei in a given local environment. Each fitted component indicated a separate population of nuclei relating to a given pore size.

T_{1A} and T_{1B} represent the relaxation time constants for the two pools of relaxation. It is noted that, during the drying process for both types of nuclei, the two pools of relaxation rate behaviour described will deplete at different rates, such that eventually it might result in a single remaining pool. In this case, a mono-exponential model was chosen to fit the relaxation data using the expression:

$$I = A - 2 * A * e^{-\tau/T_1} \quad . \quad (7)$$

2.7.2 Analysis of hp ^{129}Xe gas phase relaxation.

In order to extract the T_1 of hp ^{129}Xe the spectra were fitted to the following equation:

$$ln\frac{S_{(n)}}{S_{(n=0)}} = \left(\ln\left(cos(\theta)\right) - \frac{\tau}{T_1}\right) \cdot \mathrm{n} \quad , \quad (8)$$

where $S_{(n)}$ is the signal collected for spectrum number n, $s_{(n=0)}$ is the spectrum with the maximum intensity, and $\cos(\theta)$ is the term that accounts for the polarisation destruction from the applied r.f. pulse. This fitting was only applied to the linear region of the decay in each experiment [43]–[45]. Further, spectral information was acquired at each drying instance by the application of a 90º pulse after gas delivery.

3. RESULTS

3.1 X-ray Computed Tomography of Empty Monolith Sample

Figure 4 shows a reconstructed cross-section image of the plane perpendicular to the axis of the square channels for a typical section of the SCR monolith used in this study. Within the image, the bright white pixels correspond to the monolith walls, while the mid-grey pixels contained within the white regions are washcoat located within the monolith pores, and the dark-grey/black regions are empty pores and channels. The image of this purpose-made sample for this study shows that the washcoat material was more concentrated in the mid-sections of the channel walls, while the wall intersections/corners were relatively devoid of washcoat material, hence, were generally more porous.

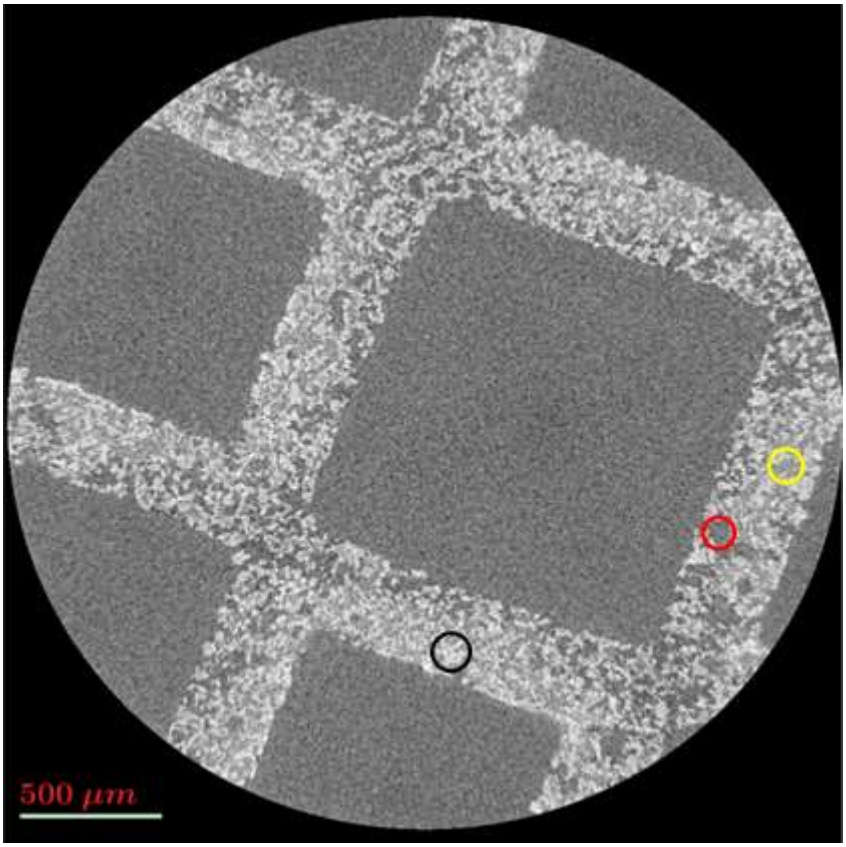

Figure 4. Reconstructed cross-section perpendicular to channels of washcoated monolith obtained from XRADIA Versa XRM-500 x-ray CT. The bright white pixels (eg black circle) are the monolith walls, the mid-grey pixels (eg yellow circle) contained within the white regions are washcoat within the monolith pores, and the dark-grey/black regions (eg red circle) are pores and channels. The scale bar corresponds to 500 mm. Resolution is 2.99 μm/pixel with a 1015 x 1015 acquisition matrix.

3.2 Mercury porosimetry

Figure 5 shows the mercury intrusion curve for the washcoated monolith following analysis of the raw data using the Kloubek correlations [38]. The initial slope of the porosimetry curve may be intrusion into large-scale surface roughness on the surface of the monolith. The main intrusion curve proper suggests three key pore size modes occurring at sizes ~10^4 nm (=10 μm), ~500 nm, and ~5 nm. These data probably correlate with three levels of porosity in the hierarchical structure of the sample, namely, (1) empty monolith pores and monolith pores

partially filled with washcoat; (2) macroporosity between zeolite crystallites in washcoat, and, third, mesopores within the binder of the washcoat material.

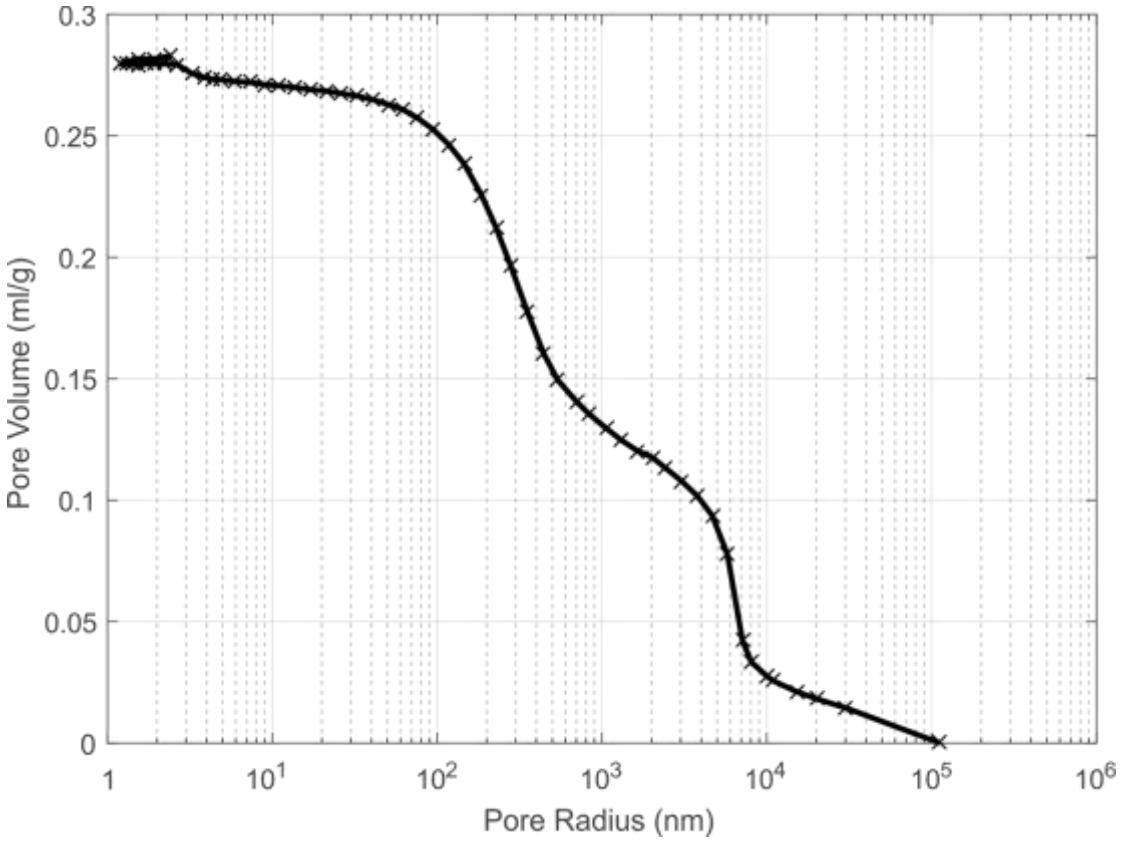

Figure 5. Mercury intrusion curve for Cu-free washcoated monolith analysed using Kloubek correlations displaying three key intrusion modes.

3.3 NMR relaxometry studies of drying

Figures 6 (a) and (b) show the fitted spin-lattice relaxation time components for ^{1}H in H_2O, and ^{2}H in D_2O, respectively, as a function of the free pore volume for variable saturation states of a monolith during a drying experiment (i.e. T_1 relaxation as a function of water contents in the monolith walls). Examples of fits to the raw relaxometry data are given in the Supplementary Material. There is no ^{1}H T_1 relaxation data from 0-30% in Figure 6(a) because in this range, the T_1 relaxation times are rather long leading to prolonged

experimental times during which the sample water content may change. For ^{1}H in H_2O, there was a slow and a fast component in the observed relaxation characterized by a long (T_1^{slow}) and a short (T_1^{fast}) relaxation time, respectively. The biexponential ^{1}H relaxation of this nuclear spin I=1/2 system in Figure 6a suggests that there are at least two regions of water with vastly different pore dimensions. Furthermore, the separate relaxation rates, associated with the two different environments, require that there is no substantial diffusion exchange between these regions within the timescale of relaxation processes. As the monolith is dried, the T_1^{slow} relaxation component accelerates and, at high free pore volume (i.e. > 55%), a stepwise drop in the relaxation rate appeared that is completed around 60% free pore volume. At even higher free pore volume, increasing beyond 60%, the T_1^{slow} component does not change significantly further and always stays well above T_1^{fast}. The short T_1^{fast} component accelerates only moderately, if at all, with growing free pore volume. According to the Brownstein-Tarr model (Eq.4), T_1^{slow} is expected for regions with larger pore sizes, while T_1^{fast} will originate from areas with more confined space in the porous hierarchy. It is apparent from Figure 6(a) that regions associated with the long T_1^{slow} component dry out first, suggesting that the largest pores dry out first, followed by a steep step when the large pores become fully depleted. Thereafter, i.e. above approximately 60%, the water associated with T_1^{slow} no longer experienced changes in the relaxation time, although the fractional water content associated with T_1^{slow} (Fig. 6a, black triangles) continued to decrease with increasing free pore volume, albeit with a reduced slope. Perhaps this is associated with water evaporating from the surface of the porous micro-crystallites. The behaviour of T_1^{fast} as a function of free pore volume, and its clear separation from the much longer T_1^{slow} times at all drying levels, suggests that it originated from water within the microporous structure within the crystallites that cannot leave this network within the timescale of the relaxation. Furthermore, the fractional water content associated with T_1^{fast} (Fig. 6a, red triangles) did not

change until about 60% free pore volume but experienced a drop at higher free pore volume. This would support the idea that, at this point, water outside the crystallites had evaporated to the extent that the drying of interior of the smallest pores became possible.

The D_2O data did not allow for a tangible bi-exponential fit, perhaps because of the less favourable signal to noise ratio compared to ^1H. It is also conceivable that the D_2O in the smallest pores is strongly broadened because of very fast quadrupolar T_2 relaxation and hence not observable. The ^2H relaxation time curve in Figure 6(b) displays a step at about 55% free pore volume, similar to the ^1H T_1^{slow} curve. This is despite the fact that the dominant relaxation mechanisms for the two types of nuclei are of fundamentally different nature, namely dipolar relaxation for ^1H, and quadrupolar relaxation for ^2H. The potency of both relaxation mechanisms would be strongly affected by the surface to volume ratio S/V as described in Eq. 4 for porous media. The relaxation data for both nuclei in Figure 6 independently suggests that one of the main step changes, during the drying process, occurring at free pore volume fraction of ~55% is indicative of the porous hierarchy of the monolith.

Paramagnetic relaxation is a mechanism that affects the observed T_1 times and the fastest relaxation will occur at close proximity to paramagnetic sites and may therefore not necessarily reflect the smallest pores within the hierarchical network. However, the highest concentration of paramagnetic sites is expected to occur within the nano-porous framework for the zeolites, i.e. within the smallest available pores. Hence, this would not change the interpretation for the cause of the observed step changes in relaxation. Nevertheless, a concern could be an unexpected high concentration of paramagnetic sites at the outer surface of the zeolite particles. However, the strength of paramagnetic relaxation would be vastly different between the two isotopes as the gyromagnetic ratio, γ, of ^2H is about 6.5 times lower compared to that of ^1H. This difference would cause an approximately 40 times longer relaxation times for ^2H due to the γ^2 dependence of paramagnetic relaxation rate. Since both isotopes show similar T_1 times,

the dominating mechanism for ^{2}H relaxation must be quadrupolar, as it cannot be explained by paramagnetic relaxation. Lastly, a similar overall relaxation behaviour for both isotopes as a function of free pore volume further supports that the observed effect is determined by *S/V* and hence the pore sizes, independent of the presence of paramagnetic sites. The porous hierarchy is further discussed in the context of ^{129}Xe relaxation data that is strongly dependent upon the accessible free pore volume at varying stages of drying.

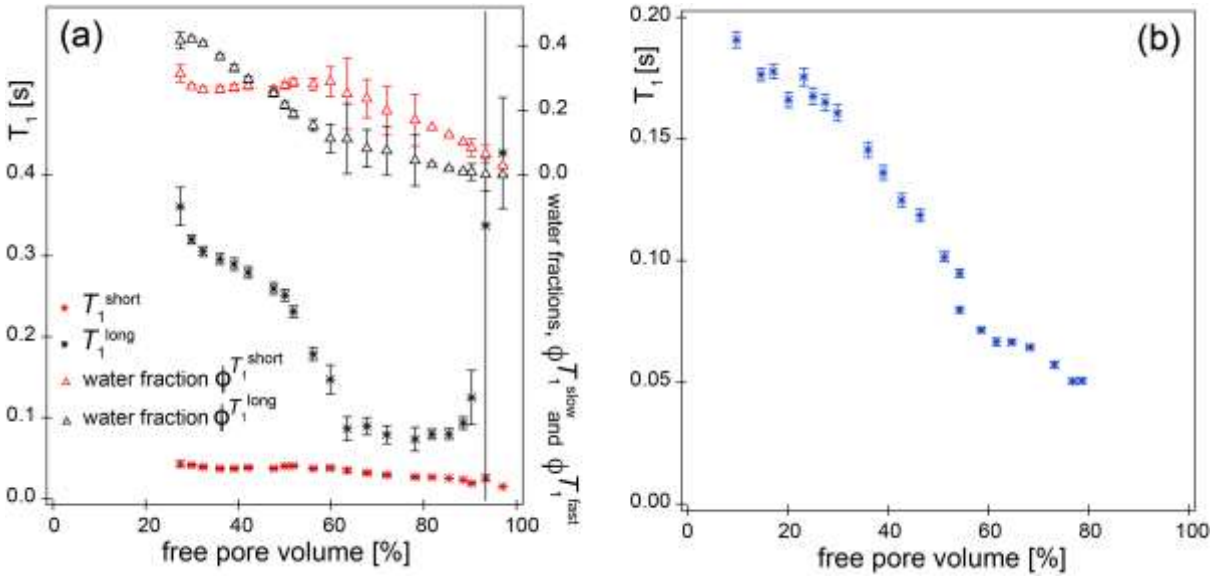

Figure 6. Spin-lattice relaxation of H_2O, (a), and D_2O, (b) as a function of the free pore volume during monolith drying experiment. Data were collected using inversion recovery method with 16 time delays. (a) The fractions $f^{T_1^{slow}}$ and $f^{T_1^{fast}}$ associated with the two ^{1}H relaxation component T_1^{slow} and T_1^{fast} determined from biexponential fitting where scaled by the total water content $\frac{(100-free\_pore\_volume)}{100}$ to provide the fractional water content $\phi^{T_1^{slow}} = f^{T_1^{slow}} \times \frac{(100-free\_pore\_volume)}{100}$ and $\phi^{T_1^{fast}} = f^{T_1^{fast}} \times \frac{(100-free\_pore\_volume)}{100}$. The average χ^2 without weighting was 0.036553 and 0.004987 for mono- and bi-exponential models, respectively. (b) T_1 values from mono-exponential fitting of the ^{2}H inversion recovery relaxation data.

3.4 Time-resolved tomographic studies of drying

Figure 7 shows time series of “unprocessed” images during drying of a monolith section. The data were collected using synchrotron-based X-ray tomography with pixel size of 0.8 μm and temporal resolution of 2 seconds. The images are cross-sections perpendicular to the monolith channels demonstrating water distribution in different stages of drying. The disappearance of the circular meniscus in the large channel of the scanned section takes place between 40-90 s, while that for the small channel disappears between 210-250 s. When the circular meniscus passes through the depicted cross-section, a water film remains in the corners of the monolith structure, which facilitates drying of the channels [46-48]. At time 390 s, the corner film in the large and the small channels vanishes and air invades the substrate wall.

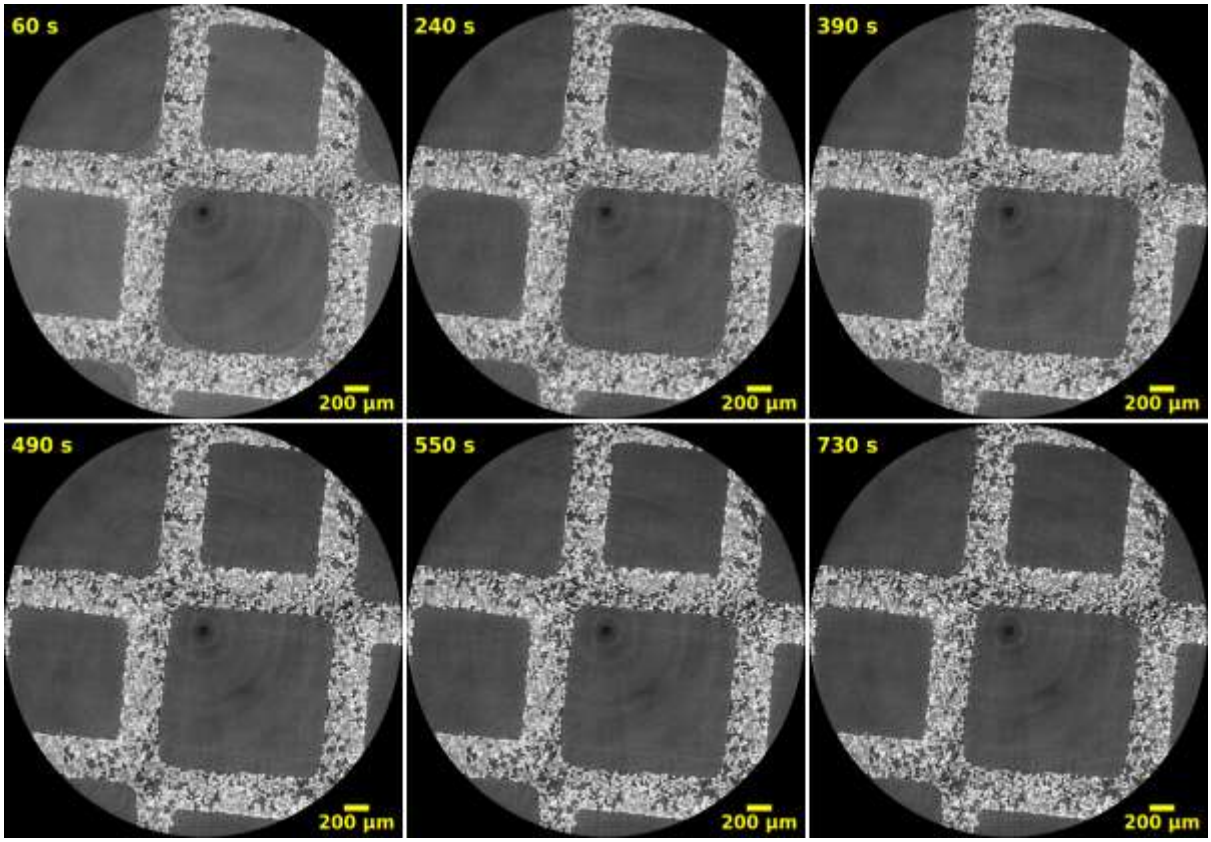

Figure 7. Drying series of "unprocessed" images (1000th slice out of 1900) of the coated monolith obtained from the synchrotron-based CT. The reconstructed cross-section is perpendicular to the channels of the sample. The bright pixels are monolith walls and Cu-zeolite coating, mid-grey pixels show water and dark are pores. The scale bar corresponds to 200 µm. The pixel size is 0.8 µm and field of view 3.2 x 1.5 mm^2. The scanning time is 2 seconds with the acquisition time indicated on each image.

To improve the contrast between water and air, the "subtracted" images were constructed by subtracting an unprocessed image at time *t* from another unprocessed image at time 0 seconds. Figure 8 depicts a time series of drying obtained by image subtraction with the brightest pixels corresponding to water removal and the darkest pixels water filling. The mid-grey levels show initial state of the sample, which includes water, unfilled pores, ceramic substrate and Cu-zeolite coating. The images, based upon the contrast variation initiated by water removal and filling, give more detailed information about the drying process compared to the "unprocessed"

images in Figure 7. During the removal of water from the asymmetric channels between 0 and 390 seconds, the porous wall remained mostly filled. The walls of the big channels, in the cross-section studied, were exposed at 230 seconds, with only a water film remaining in the corners, as seen in Figures 8 and 9. However, the air did not invade the wall structure before 390 seconds. As the evaporation took place at all air-water interfaces, including the exposed big channels, this implies that water is constantly pumped by capillary forces to refill the porous walls. Figures 8 and 9 show that some pores within the monolith wall emptied (bright pixels), while other pores filled (dark pixels), during the drying of the channels between 0 and 390 second, which further hints at water transport through the porous wall.

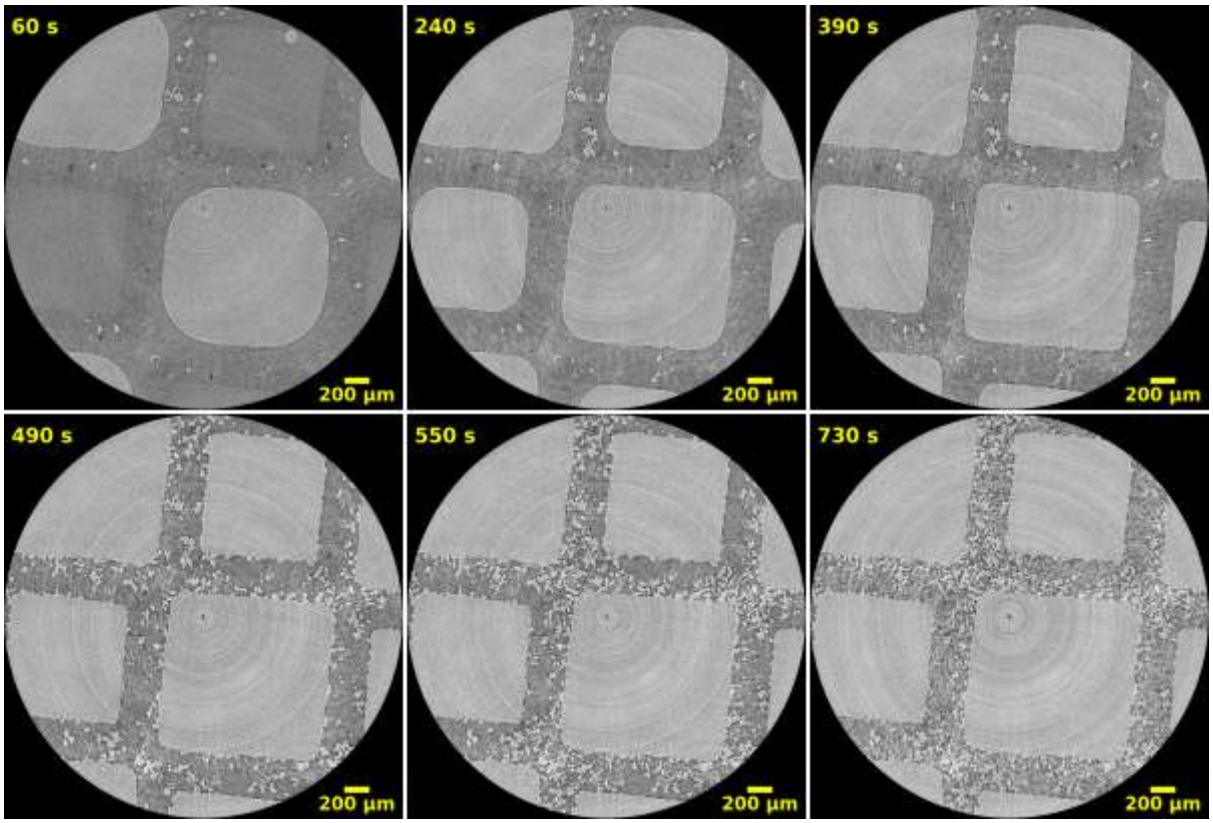

Figure 8. Drying series of "subtracted" images (1000th slice out of 1900) of the coated monolith obtained from the synchrotron-based CT. The reconstructed cross-section is perpendicular to the channels of the sample. The images show contrast variation between 0 second and time *t* indicated on each image: the bright pixels correspond to water removal and the darkest pixels water filling. The mid-grey pixels show initial state of the sample, which

includes water, unfilled pores, ceramic substrate and Cu-zeolite coating. The scale bar corresponds to 200 μm. The pixel size is 0.8 μm and image size 3.2 x 3.2 mm^2. The scanning time is 2 seconds.

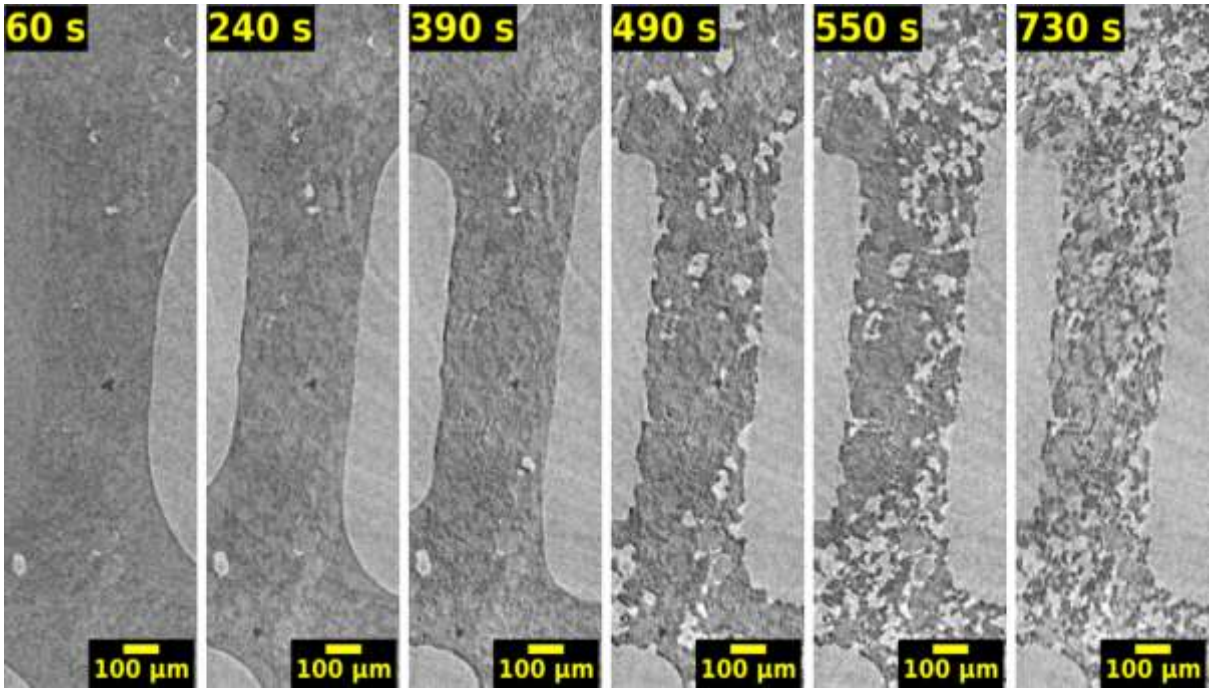

Figure 9. Detailed view of a cross-section perpendicular to the monolith channels during drying. The images obtained from the synchrotron-based CT are "subtracted" to follow the contrast variation between time 0 seconds and time *t* indicated on each image. The brightest pixels correspond to water removal and the darkest pixels water filling. The mid-grey pixels show initial state of the sample, which includes water, unfilled pores, ceramic substrate and Cu-zeolite coating. The scale bar corresponds to 100 μm. The pixel size is 0.8 μm and image size 0.48 x 1.6 mm^2. The scanning time is 2 seconds.

The "subtracted" images were re-sliced, to investigate the onset of the air invasion into the porous wall along the monolith channel, to give Figure 10 and detailed view in Figure 11. The monolith wall was exposed to air from approximately 60, or 230, seconds on the side of a big, or a small, channel, respectively. The meniscus receded within the captured section of the

monolith sample in the direction of from bottom to top. The water meniscus did not invade the wall structure along the entire length of the scanned section until 390 seconds, which corresponded to the disappearance of the water film from the corners of the monolith structure, as seen in Figures 8 and 9. As the re-sliced images cut the monolith sample through the centre of the channels, the corner film cannot be seen in Figures 10 and 11. Once the air invaded the walls, the drying front proceeded mainly from the side of the big channel and towards the monolith corners, as seen in Figures 9 and 11. The side of the small channels, which was occupied with Cu-zeolite, remained filled with water. The small size of the pores within the wash-coating (as observed by mercury intrusion in Figure 5) thus indicates that water transport from the big pores of the monolith structure occurred by capillary pumping. At time 550 seconds, no movement of water is visible in the wall porosity.

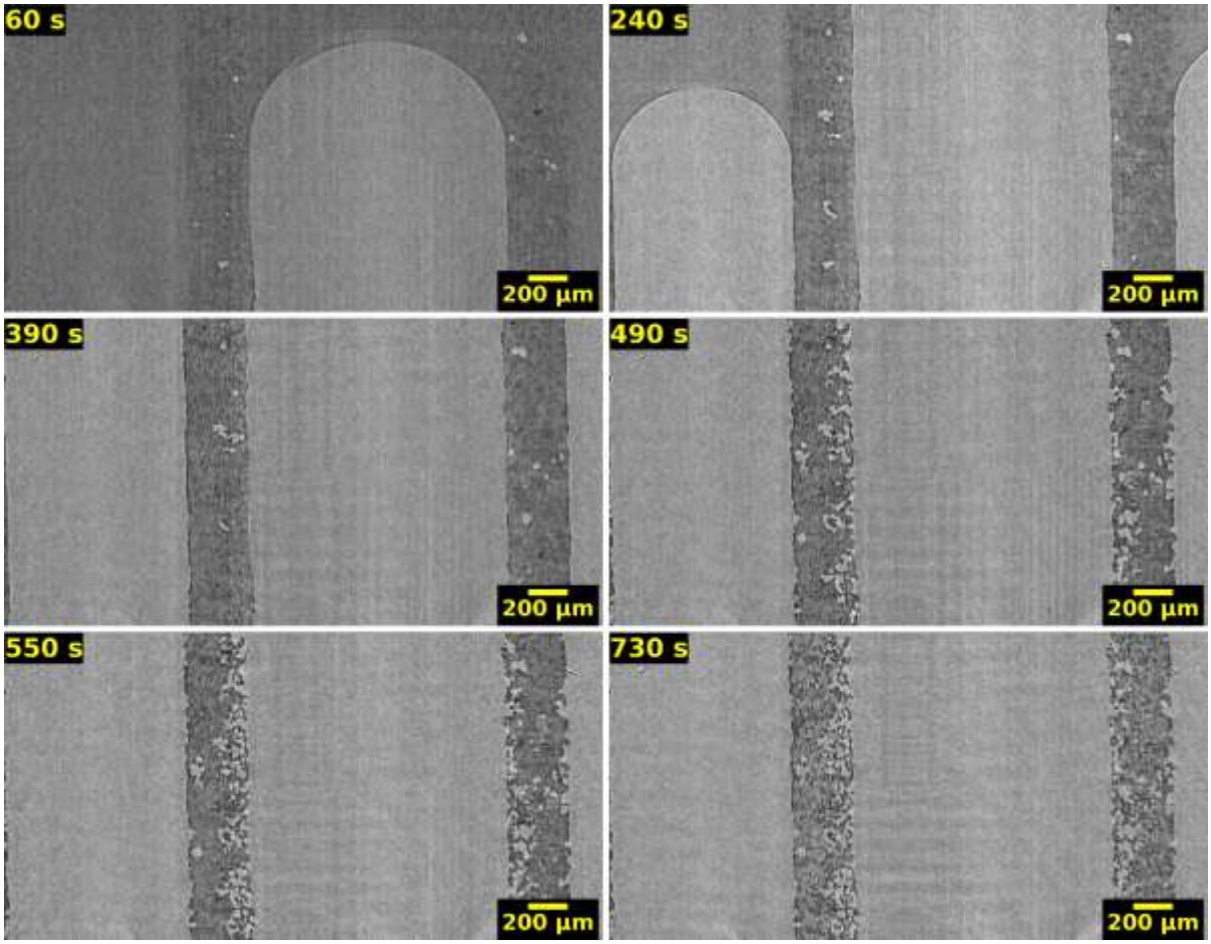

Figure 10. Drying series of "subtracted" images resliced along the monolith channel obtained from synchrotron-based CT. The plane showed here cuts through the centre of asymmetric channel structure. The images depicts contrast variation between 0 seconds and time *t* indicated on each image: the bright pixels correspond to water removal and the darkest pixels water filling. The mid-grey pixels show initial state of the sample, which includes water, unfilled pores, ceramic substrate and Cu-zeolite coating. The scale bar corresponds to 200 µm. The pixel size is 0.8 µm and image size 3.2 x 1.6 mm^2. The scanning time is 2 seconds.

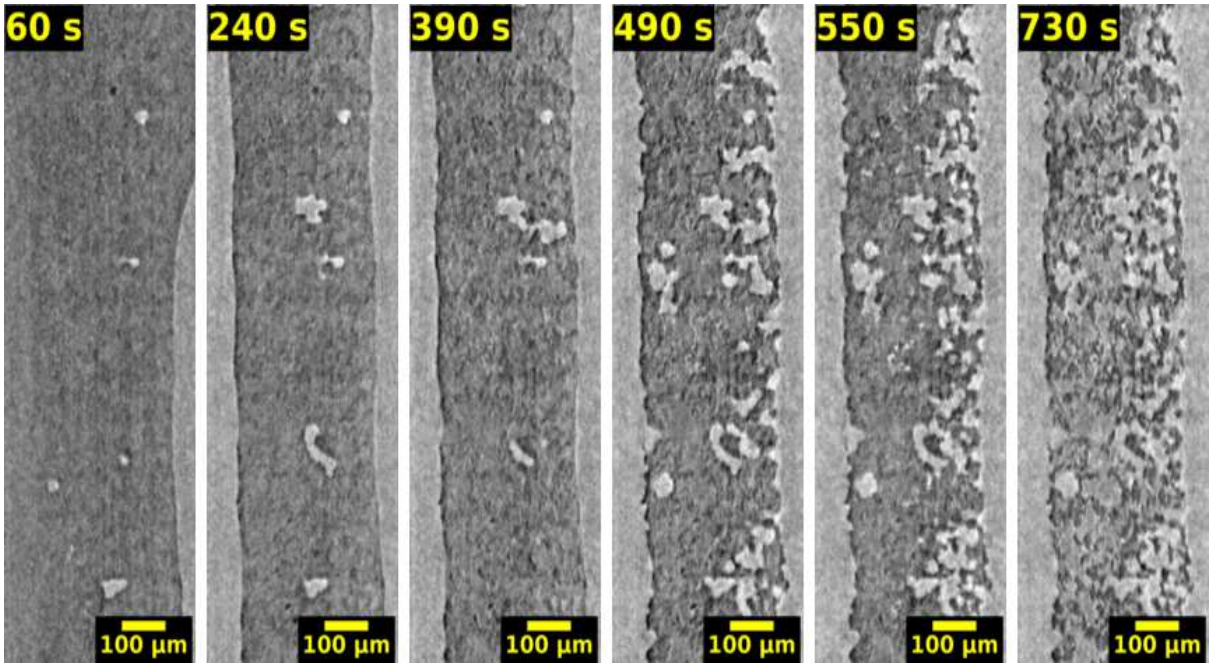

Figure 11. Detailed view of a wall section along the monolith channel during drying. The images obtained from the synchrotron-based CT are "subtracted" to follow the contrast variation between time 0 seconds and time *t* indicated on each image. The bright pixels correspond to water removal and the darkest pixels water filling. The mid-grey pixels show initial state of the sample, which includes water, unfilled pores, ceramic substrate and Cu-zeolite coating. The scale bar corresponds to 100 µm. The pixel size is 0.8 µm and image size 0.48 x 1.6 mm^2. The scanning time is 2 seconds.

As the pores of the Cu-zeolite coating are below the resolution limit of the synchrotron-based CT, direct, pore-scale resolved information about the drying process cannot be obtained. However, the amount of water within the coating affects the transmission of the X-ray beam. The contrast variation, thus, reveals information about the drying process below the spatial resolution, as seen in Figure 12. The averaged pixel intensity of the wall region does not change during drying of the monolith channels before 390 seconds. When the air invaded the monolith wall, the observed contrast increased as water was removed from the big pores, as seen in Figures 9 and 11. At time 550 seconds, water movement was no-longer visible in the resolved pores of the walls. However, the averaged pixel intensity continued to rise as water was

removed from the Cu-zeolite coating. After 730 seconds, the then invariant contrast curve indicated the end of the drying process.

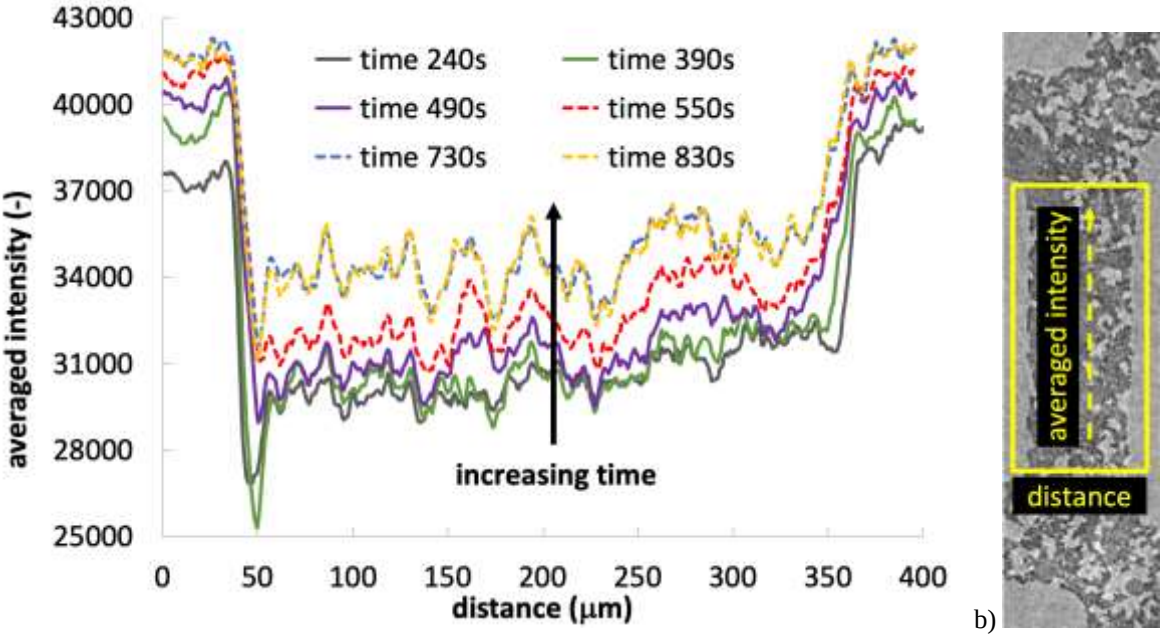

a) b)

Figure 12. a) Averaged pixel intensity across the wall with Cu-zeolite coating as indicated by the yellow rectangle in (b). The solid lines correspond to drying of monolith channels and big pores resolved by synchrotron-based CT. The dashed lines show drying of the Cu-zeolite coating when no visible movement of water is observed in the resolved pores.

A consideration of the synchrotron-based CT data, given in Figures 7-12, suggests a general description of the drying process. Water evaporated from the coated monolith structure in the following hierarchical order from big to small pores:

1) Bulk water from the big channels of the asymmetric structure. Water film remains in the corners of the monolith.
2) Bulk water from the small channels leaving behind water film in the corners.
3) Water film in the corners of big and small channels.
4) Water in the big pores of the monolith wall.
5) Water in the Cu-zeolite wash-coating.

3.5 ^{2}H MRI studies of drying of monolith

Figure 13 shows gradient echo spin density images for axial cross-sections of the monolith at different $^{2}H_2O$ saturations during a drying experiment. Deuterated water was used for this experiment as $^{2}H_2O$ is relatively insensitive to the chemical heterogeneity in the form of paramagnetic sites (see section 3.3). From a comparison of the images for spin density, which is directly proportional to $^{2}H_2O$ content, it can be seen that, at full saturation, i.e. 0% free pore volume, the highest concentration of (heavy) water is present within the highly porous intersections, with relatively less in the walls. After drying to 54% free pore volume the intersections have been partially depleted of water. Further, at free pore volumes 68% and 77%, the majority of the remaining liquid can be found within the walls of the monolith with decreasing water signal arising from the intersections. This confirms the observation from the CT data that the intersections dry out before the walls.

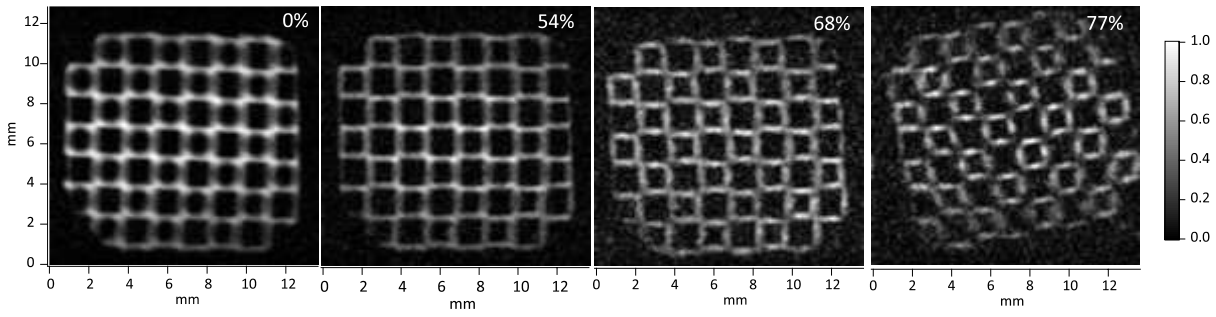

Figure 13. D_2O spin density images for axial cross-sections of monolith at different levels of monolith saturation with D_2O during drying. Monolith saturation with D_2O was determined from the areas of one-dimensional spectra acquired during monolith drying before image collection. Each image is normalised to the highest intensity for visualisation of sites filled with D_2O during drying. The scale to the right indicates the progression of colours from the lowest (0) to the highest (1) intensity in images.

Figure 14(a) depicts spin-echo images of a SCR monolith fully saturated in D_2O collected at two different τ delay times. The interpolated intensity map and T_2 relaxation map reconstructed from exponential analysis of each voxel using eight τ delays are shown in Figure 14(b). A thresholded spin-spin (T_2) relaxation map and associated histogram of T_2 values along with bimodal gaussian decomposition are shown in Figure 14(c). From Figure 14 (c), it can be seen that the longest T_2 values are located within the intersections of the walls, having a value of ~ 19 ms while a shorter component of ~18 ms is located within the walls and the presence of bi-modal distribution is demonstrated by the deconvolution of T_2 histogram lineshape with two gaussians (Figure 14(c)). Since the Brownstein-Tarr relationship (Eq.(4)) suggests that, when fluids are relaxing within porous media longer relaxation times are associated with larger pores, then the largest pores are located in the intersections. Hence, these MRI data are consistent with the data reported above from CT displayed in Figure 4.

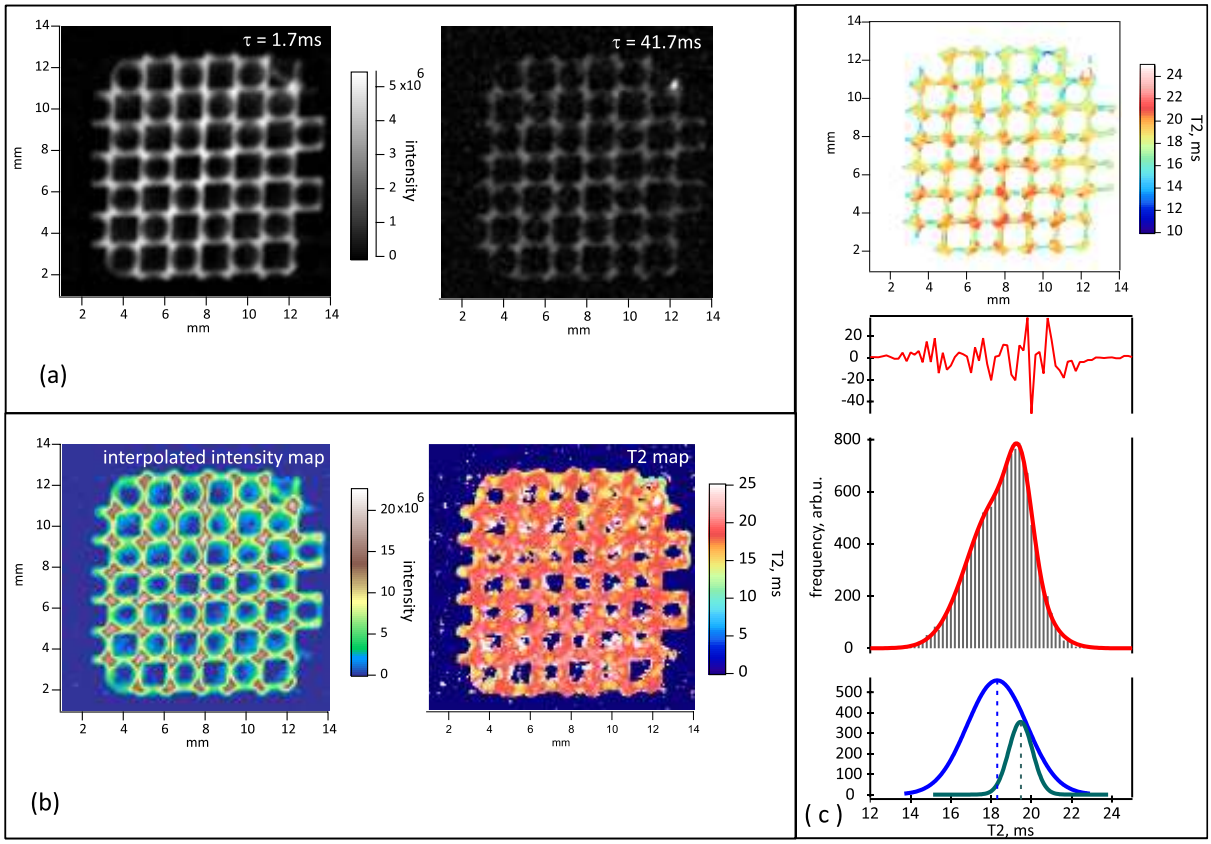

Figure 14. (a**) –** ^{2}H spin echo intensity maps of an axial cross-section of monolith fully saturated in deuterium oxide acquired at τ = 1.7ms and τ = 41.7ms. (b) An interpolated intensity image calculated from exponential analysis of spin density images acquired at eight τ delays and a corresponding T_2 relaxation map of D_2O in fully saturated monolith. (c) A thresholded T_2 map and the corresponding histogram of T_2 values in this map fitted to bi-modal gaussian function. Individual deconvoluted gaussians are also shown with their mean values indicated by dashed lines.

3.6 hp ^{129}Xe NMR relaxometry studies of drying of monolith

Figure 15(a) shows a schematic of the sample used for this series of experiments. The hp xenon gas was vacuum shuttled into the sample container holding the monolith segment. As the findings above demonstrate, during the drying procedure the moisture progressively left successive levels in the hierarchy of the pore structure. At the very lowest moisture contents (high free pore volumes) the smallest level of the pore structure was opened, thus allowing hp

xenon gas to enter the smallest pores and experience a chemical shift of ~89 ppm as shown in the spectrum in Figure 15(b).

Figure 16 shows the spin-lattice relaxation times for hyperpolarised ^{129}Xe in the gas phase located in the progressively increasing free pore volume of partially saturated samples during the drying experiments. Note, that ^{129}Xe in the pure gas phase, i.e. in the absence of high surface areas, typically displays T_1 times of 1–2 hours and the relaxation times shown in Figure 16 originated therefore exclusively from the surface interactions. Close proximity to paramagnetic surface sites will significantly shorten the observed ^{129}Xe T_1 due to the r^{-6} dependence of paramagnetic relaxation on the distance r of the nuclear spin to the site. It can be seen that these data show three main step changes in T_1 at free pore volume fractions of ~20, ~60 and ~90 %. The one at 60% is similar to the corresponding positions of the main step in the relaxation data for water and heavy water in Figure 6. Hence, relaxation time data from all three different nuclei all indicate that the drying of the monolith pore structure proceeds in a hierarchical fashion, with the largest pores drying out first, followed by intermediate, and then smaller pores. At the final free pore volume fraction step (~90 %) the pore structure is sufficiently open for the hp ^{129}Xe gas to enter the smallest level of pores that causes a second peak to appear (see Figure 15b). Note that at this point the relaxation of the ^{129}Xe gas phase signal is very high and leads to a rapid decay of the ^{129}Xe hyperpolarized spin state.

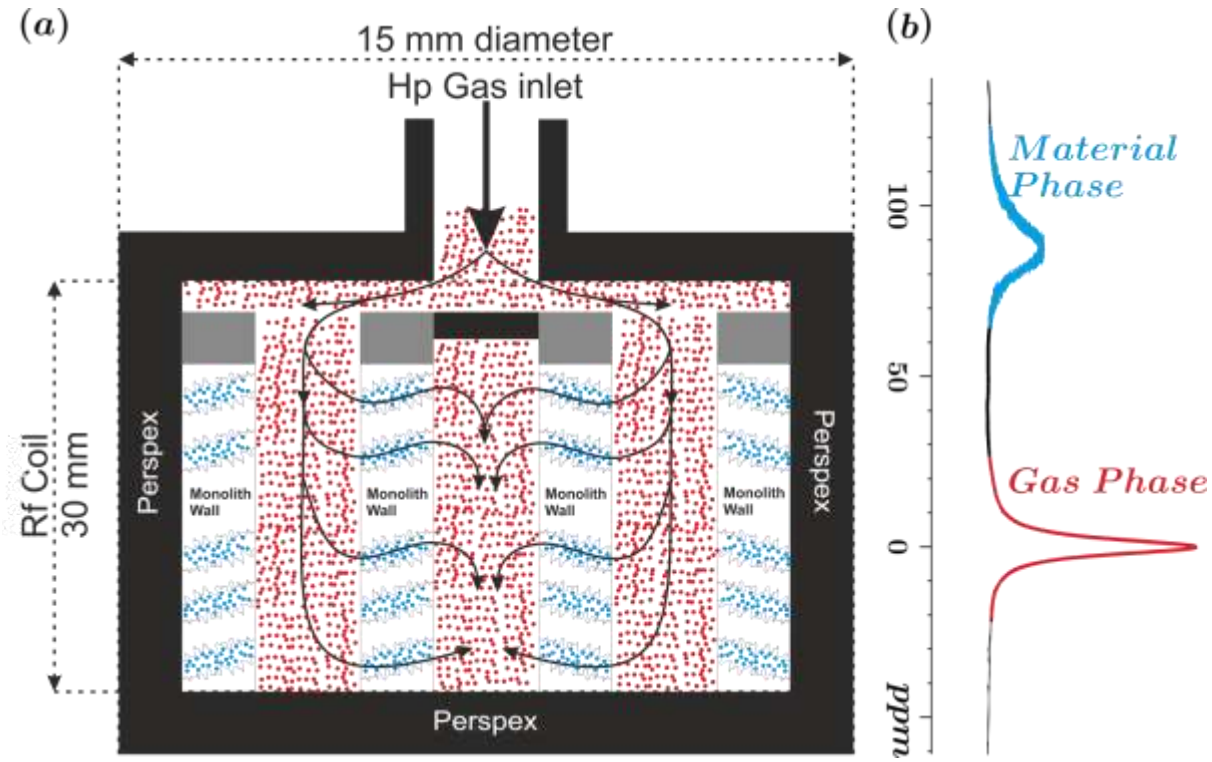

Figure 15. (a) Schematic of the Sample used in the Relaxation experiments. As the hp ^{129}Xe gas enters the monolith it is unbound in the *gas phase* (red circles) where as it moves through the porous monolith walls the hp ^{129}Xe experiences a large chemical shift in this state (blue circles) as indicated in the spectra in (b). **(b)** hp ^{129}Xe 1-D spectrum of gas in the monolith structure. The chemical shift separation between gas phase (red) and the imbibed phase (blue) is 89 ppm. The spectra is comprised of a single acquisition with the RF carrier frequency set between the two peaks to ensure even excitation.

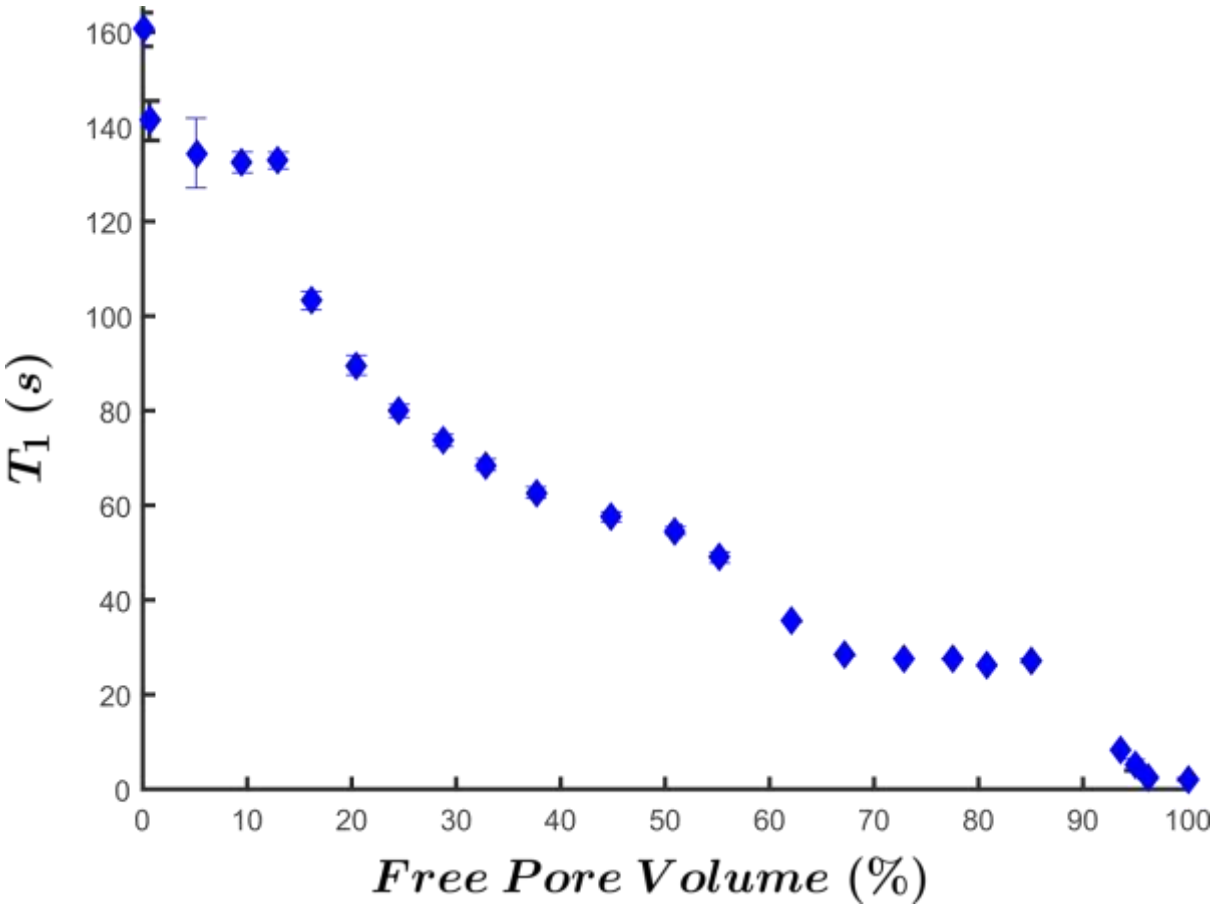

Figure 16. Variation in spin-lattice relaxation times for hyperpolarised ^{129}Xe with changing free pore volume of partially saturated samples during drying experiments. The data were acquired by a train of low flip angle pulses, as described in the main text. Each data point represents four averaged data points with the error bars indicating the standard error of the datasets for the T_1 relaxation time and the calculated free pore volume of each individually collected dataset.

3.7 MRI studies of xenon diffusional permeation at variable saturation levels

Figure 17 shows a schematic diagram depicting the pattern of gas flow within the SCR monolith segment used in this series of experiments. The hp ^{129}Xe gas flowed into a single channel with a blocked far end. Therefore, in order to exit the monolith segment, the hp gas was forced to cross through the monolith porous wall or intersection structures.

The hp ^{129}Xe MR images obtained with this setup are depicted in Figure 18, which visualizes the spatial dispersion of xenon at different water saturation levels of the monolith sample. The contrast in the images was obtained through the selection of different repetition (or recycle) times, TR. Unlike conventional ^{1}H MRI with a static fluid where an alternation of TR changes the extent of T_1 recovery and therefore leads to T_1-weighted images, TR changes in a flowing system may lead to fluid transport weighted images. This is the case for ^{1}H MRI under flow conditions if the flow outpaces the T_1 relaxation and the fluid had been pre-polarized in the high magnetic field region before entering the detection zone. In the case of hyperpolarized ^{129}Xe, where spin exchange optical pumping always takes place outside the sample (and even outside the high field region of the superconducting magnet), transport is required for a signal to be observed. The hyperpolarized state of ^{129}Xe in the images shown in Figure18 was destroyed by each applied 90° radiofrequency pulse and hp ^{129}Xe therefore needed to be replaced for each scan. Note that T_1 relaxation will not produce hp ^{129}Xe signal recovery as T_1 relaxation causes reinstatement of the thermal equilibrium that is orders of magnitude weaker than the hyperpolarized state and hence will only lead to a weakening of the signal (i.e. negative MRI contrast).

Under continuous flow conditions, as was applied here, the transport into and through the sample takes place through flow and diffusion. Figure 18 shows how with increasing transport time (horizontal-axis) the xenon moved away from the central channel location of gas injection. These transport-weighted, or flow- and diffusion-weighted, images were repeated for different water saturations (i.e. different free pore volumes; vertical-axis). Initially, at very low free pore volume (5 %), the images suggest a film of water was present within the corners of the monolith causing the channels to appear cylindrical, which is in agreement with the $^{2}H_2O$ MRI at 0% free pore volume shown in Figure 13. At the low free pore volume of 5%, permeation crosses over from the single inlet channel to the adjacent exit channels but further permeation appears

biased towards the highly porous corners of the channels as xenon was absent from most adjacent channels (i.e. half of the channels are 'dark' or without xenon). At intermediate saturation levels, starting form 20% free pore volume through 55%, hp ^{129}Xe is now observed in adjacent channels, providing evidence of overall flow in directions perpendicular to the channel walls. This indicates that flow though the walls may occur, although propagation across the highly porous corners can also lead to transport between adjacent channels and this route is supported by the observations from $^{2}H_2O$ MRI at 55% free pore volume shown in Figure 13. It is noted that the aforementioned relaxation time data, from the drying experiments, suggests that the intermediate-sized porosity is emptied of water in the drying step at free pore volumes of ~55 %. However, the then availability of the intermediate-sized porosity for mass transport does not appear to lead to a corresponding increase in the spreading rate of the hp ^{129}Xe permeation front through the pore structure. Note also, that at all saturation levels up to 55%, the dispersion pattern of the gas with increasing time lacks overall symmetry, thereby suggesting the distribution of porosity (and thence the distribution of washcoat within the monolith) through which it flows is heterogeneous. At very high free pore volumes (i.e. 82% and higher), where the drying curves suggested the smallest pore size were opened up, the intensity of the hp ^{129}Xe signal then drops substantially. The very fast relaxation observed in Figure 16 at very high pore volumes caused the hp ^{129}Xe to depolarize very rapidly, leading to thermally polarized ^{129}Xe that does not produce sufficient signal intensity to be observed in the MRI, despite ongoing gas transport. The hp ^{129}Xe MRI signal disappeared when the smallest pores with highest *S/V*, and paramagnetic sites within these pores, became accessible. Since the high *S/V* region and paramagnetic centres are associated with the catalytically active phase, this suggests that the catalyst is only largely accessed once molecules penetrate the smallest level in the pore size hierarchy in the drying curves. The disappearance of the hp ^{129}Xe MRI signal outside the entry channel at the centre may therefore reflect the reactivity of monolith.

Beyond this qualitative statement, future work is needed to quantify how the relaxivity of a porous medium for ^{129}Xe also reflects reactivity of this medium for other gases. Remarkably, not all the hp ^{129}Xe signal outside the entry channel disappeared as can be seen for long transport times for 82%, and to a lesser extent for 97%, free pore volume. The hyperpolarization clearly survived transport between channels, probably caused by transport through the highly porous corners (i.e. wall intersections) that are largely void of the catalyst. This shows that a route to bypass the catalytic active region exists even at very high free pore volume.

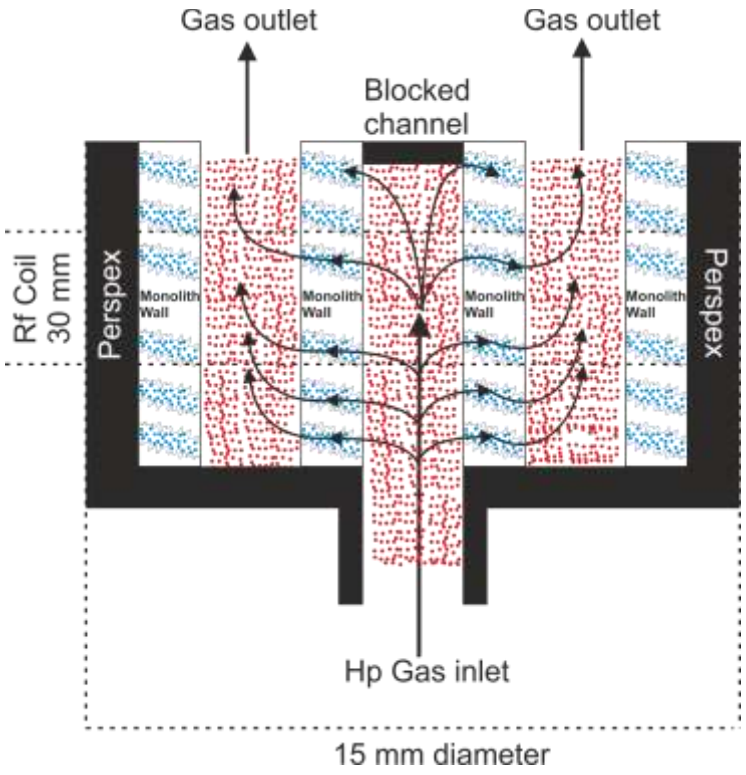

Figure 17 Schematic depiction of the flow pattern within a monolith segment with gas delivered to a single channel of the SCR filtration monolith. The hp ^{129}Xe enters the central, blocked far-end channel, and, thence, is forced to move through the substrate walls so as to escape the monolith. The outer walls and the bottom of the monolith was wrapped with Parafilm such that the only exit for the gas was that of the open channels at the top of the monolith.

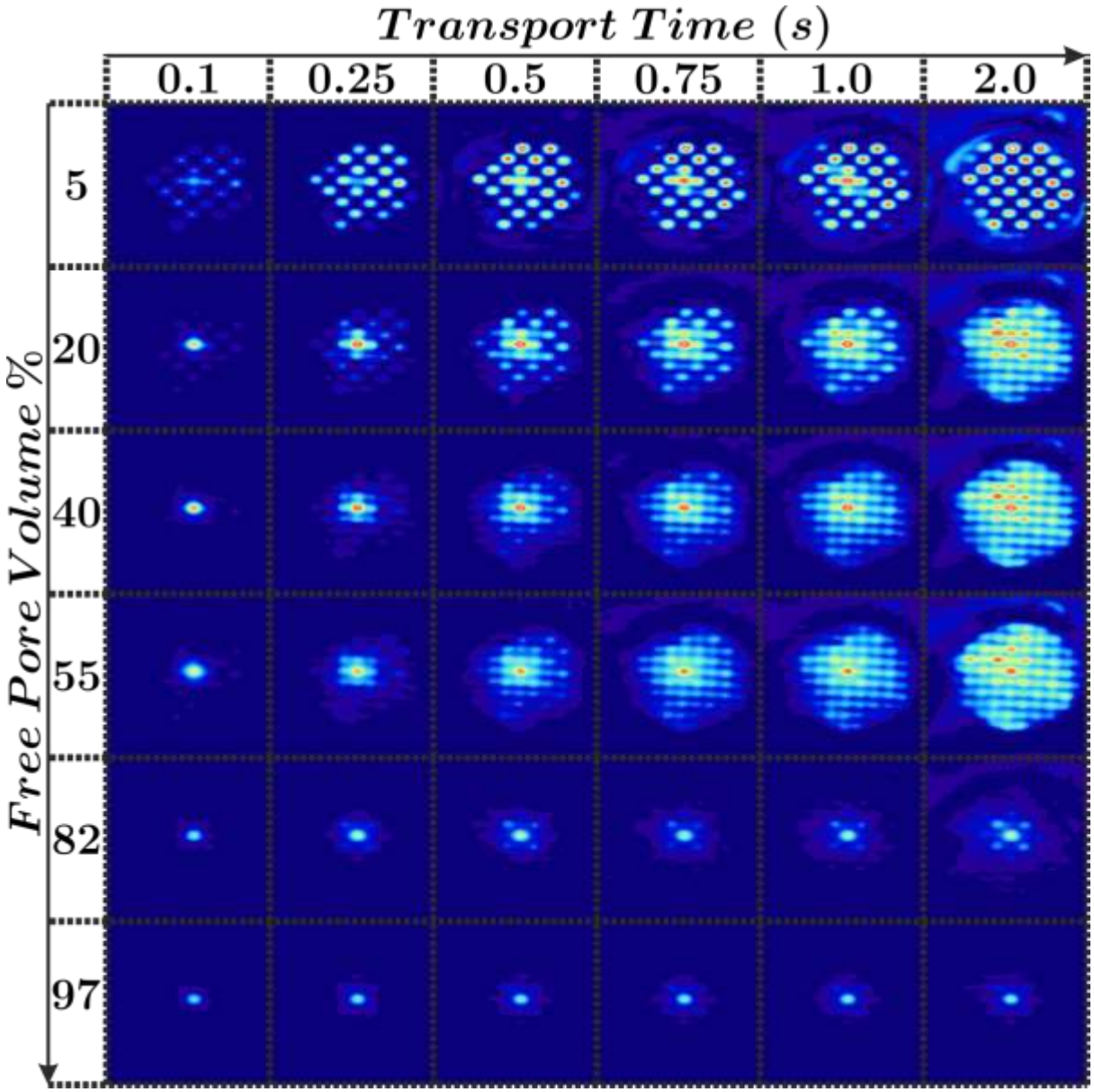

Figure 18. Two-dimensional spin density images of the the spatial dispersion of hp ^{129}Xe, within an axial cross-section of a combined SCR filtration monolith, with increasing transport time. High gas density is indicated by red colours, and lower densities are indicated by yellow to blue colours. Gas flowed at a constant rate through a single channel of the SCR monolith after it has been saturated in distilled water. The images were acquired by a standard gradient echo sequence. The hp gas replenishment delay was varied so as to provide an insight into the dispersive mass transfer from the delivery channel to the outlying channels. The acquisition matrix was 64 × 32, zero filled to 128 × 128, FOV read: 22.1 mm, FOV phase: 16.99 mm, FOV slice: 15.7 mm. The water in this series of experiments was used to occlude pathways within the SCR monolith's pore structure so as to reduce the effects of paramagnetic relaxation, and illustrate the flow

pathways within the monolith pore structure. The drying was provided by the flow of the hp gas during the imaging experiment and molecular nitrogen when not imaging.

4. DISCUSSION

Mercury porosimetry data has demonstrated that the washcoated monolith has a hierarchical pore structure with three clear pore size modes. The sizes of these modes suggest that they belong to the large empty macropores in the monolith substrate, the macropores in the washcoat formed by the spaces left around the zeolite crystallites, and the mesopores in the binder in the washcoat. The CT data suggests that the empty macropores in the monolith, and thence the regions of highest porosity, are predominantly located in the wall intersections, rather than the walls proper themselves. This claim is supported by the T_2 map of the fully saturated sample, suggesting the largest pores are found within the wall intersections. However, a portion of empty macropores has been found by CT mostly in the proximity of the big channel indicating that the SCR washcoat entered from the small channel during the coating process.

The *in-situ* CT results, and the NMR relaxometry studies of drying, both those using the liquid still imbibed in the pores, and that using hp ^{129}Xe gas imbibed into the empty voids, all suggest that the largest pores in the washcoated monolith dry out first, followed by the intermediate sized pores, and finally the smallest pores. Thence, the water saturation level can be used to selectively block particular levels in the pore network hierarchy, namely; all pores; intermediate and small pores; or only small pores. Further, hp ^{129}Xe may be used to probe the smallest level of the pore hierarchy when the moisture content of $^{1}H_2O$ or $^{2}H_2O$ proves insufficient for signal detection.

This work has assessed the impact on mass transport of the relative resistances presented by the pores in the different levels of the network hierarchy. The aforementioned method used has blocked off the various pores in the hierarchy entirely and progressively opened them up, such that the impact of the presence of particular levels of pores, or not, on mass transport can then be assessed. Such a gross effect is likely to be largely independent of the transport mechanism, or absolute value of diffusivity, in a given set of pores. However, in Knudsen diffusion, the single pore resistance depends upon the cube of the pore size, while that for molecular diffusion only depends upon the square, so low density gas mass transport is more sensitive to the differences in pore size. For the same gas, under the same conditions of temperature and pressure, the relative difference in Knudsen diffusivity between pores depends only upon the ratio of their pore sizes. The conditions of the xenon permeation experiments are lower in absolute temperature (by factor of ~2) than the typical operating conditions for the catalysed DPF but the relative sizes of the Knudsen diffusivities in the different pores will be the same, since this only depends upon pore sizes. Hence, the relative impact of different levels of the pore hierarchy on Knudsen diffusivity will be comparable under the experimental and operational conditions.

As mentioned above the working catalysed DPF typically operates at conditions of ~150-400 °C and 1 atm, when the mean free path (for nitrogen) is typically ~135-215 nm, which is of the same order in size, or greater than, the first two pore size modes in the mercury porosimetry data. Hence, during operation, diffusion in these pores will be in the Knudsen or transitional regime, while that in the third, and largest, mode will be molecular. The MRI mass transport experiments were conducted at conditions such that the mean free path was ~100 nm and thus, since this is still of the same order in size as that during operation and the broad second mode, the diffusion would also be Knudsen or transitional regime in the first two pore size modes.

Experiments could potentially be conducted at elevated temperatures. A number of studies expose hyperpolarized noble gases to high temperature reaction zones, for example for the study of catalytic hydrogenation [21], for MRI of the gas dynamics in combustion zones [19, 49], and during catalytic hydrogen combustion for the purification of the hp noble gases during the production of these MRI contrast agents [18]. These types of experiments are possible because hp ^{129}Xe, produced through the laser pumping process, has extremely low spin temperature around 10^{-2} K that is preserved in thermal environments with 5 order of magnitude higher temperatures as long as the T_1 relaxation time is longer as the transport processes involved. It is therefore conceivable that hp ^{129}Xe could be added into diesel engine exhaust for *in situ* studies of catalysed diesel particulate filter. Other, perhaps simpler arrangements could heat the gas in a heat exchanger to produce conditions that resemble those during typical operation. This will be the subject of a future work.

The transport weighted hp ^{129}Xe MR images suggest that the higher porosity and larger pore sizes in the regions at the wall intersections make the greatest contribution to overall mass transport at low free pore volume. These studies also indicated that even when the intermediate pores, located predominantly in the walls proper, are open, they make a relatively lesser contribution to mass transport. Hence, even though the monolith macropores only represent about a third of the overall pore volume in the mercury porosimetry data, they dominate the overall pattern of mass transport under these conditions. The ^{129}Xe T_1 relaxation dependence on the accessibility of the porous hierarchy, found in the static measurements, explains a further observation under continuous flow conditions, namely that, at lower moisture content, the hp ^{129}Xe MRI signal largely, but not completely, disappears. The hp ^{129}Xe MRI signal largely, but not completely, disappears when all pores, including the catalytic active sites become accessible. Future work will need to quantify how relaxivity of monoliths for ^{129}Xe reflects their actual reactivity for other gases. However, the remaining hp ^{129}Xe MRI signal, observed

in the monolith with highest free pore volume, qualitatively suggests that the distribution of the mass transport flux within the overall pore network is likely to lead to partial bypassing of the regions of that network that contain catalyst.

5. CONCLUSIONS

It has been found that the washcoat of a SCR monolith catalyst is predominantly located in the channel walls, rather than the intersections. The macro-/meso-pore network structure is hierarchical and possesses three distinct levels of pore sizes. The largest sizes in the hierarchy are predomnantly located in the channel wall intersections, with the intermediate and smallest sizes located in the walls. The hp xenon MRI permeation experiments on progressively drying samples have shown that even when the intermediate level in the pore network hierarchy has been opened, the mass transport is still dominated by the fluxes through the largest pores in the channel wall intersections. The xenon relaxation has shown that it is only when the gas can access the smallest level in the pore size hierarchy that substantial access to the catalytically-active phase is obtained. The pattern of mass transport behaviour thus suggests the potential for substantial bypassing of the catalyst.

Acknowledgements

FHC, SPR, GP and TM thank Johnson Matthey and the University of Nottingham for financial support. VN acknowledges funding from the European Union's Horizon 2020 research and innovation programme under the Marie Skłodowska-Curie Grant Agreement No 701647. We

acknowledge the Paul Scherrer Institute, Villigen, Switzerland for provision of synchrotron radiation beamtime at the TOMCAT beamline X02DA of the SLS.

REFERENCES

[1] P. Yu, X. Zhao, Y. Li, and Q. Zhang, "Controllable growth of polyaniline nanowire arrays on hierarchical macro/mesoporous graphene foams for high-performance flexible supercapacitors," *Appl. Surf. Sci.,* 393 (2017) 37–45.

[2] W. F. Lai, A. S. Susha, and A. L. Rogach, "Multicompartment Microgel Beads for Co-Delivery of Multiple Drugs at Individual Release Rates," *ACS Appl. Mater. Interfaces,* 8 (2016) 871–880.

[3] A. Śrebowata, K. Tarach, V. Girman, and K. Góra-Marek, "Catalytic removal of trichloroethylene from water over palladium loaded microporous and hierarchical zeolites," *Appl. Catal. B Environ.* 181 (2016) 550–560.

[4] C. Fang, L. Shi, H. Li, L. Huang, J. Zhang, and D. Zhang, "Creating hierarchically macro-/mesoporous Sn/CeO_2 for the selective catalytic reduction of NO with NH_3," *RSC Adv.* 6 (2016) 78727–78736.

[5] X. Wen, D. Zhang, L. Shi, T. Yan, H. Wang, and J. Zhang, "Three-dimensional hierarchical porous carbon with a bimodal pore arrangement for capacitive deionization," *J. Mater. Chem.* 22 (2012) 23835.

[6] X. Wen, D. Zhang, T. Yan, J. Zhang, and L. Shi, "Three-dimensional graphene-based hierarchically porous carbon composites prepared by a dual-template strategy for capacitive deionization," *J. Mater. Chem. A* 1 (2013) 12334.

[7] P. Kočí, M. Isoz, M. Plachá, A. Arvajová, M. Václavík, M. Svoboda, E. Price, V. Novák, D., and Thompset, "3D reconstruction and pore-scale modeling of coated catalytic filters for automotive exhaust gas aftertreatment," *Catal. Today* 320 (2019) 165–174.

[8] A. Nepryahin, E. M. Holt, R. S. Fletcher, and S. P. Rigby, “Structure-transport relationships in disordered solids using integrated rate of gas sorption and mercury porosimetry,” *Chem. Eng. Sci.* 152 (2016) 663–673.

[9] I. V. Koptyug, R. Z. Sagdeev, L. Y. Khitrina, and V. N. Parmon, “A nuclear magnetic resonance microscopy study of mass transport in porous materials,” *Appl. Magn. Reson.* 18 (2000) 13–28.

[10] I. V. Koptyung, A. V Matveev, and S. A. Altobelli, “NMR studies of hydrocarbon gas flow and dispersion,” *Appl. Magn. Reson.* 22 (2002) 187–200.

[11] M. D. Mantle, A. J. Sederman, L. F. Gladden, S. Raymahasay, J. M. Winterbottom, and E. H. Stitt, “Dynamic MRI visualization of two-phase flow in a ceramic monolith,” *AIChE J.* 48 (2002) 909–912.

[12] N. P. Ramskill, L. F. Gladden, A. P. E. York, A. J. Sederman, J. Mitchell, and K. A. Hardstone, “Understanding the operation and preparation of diesel particulate filters using a multi-faceted nuclear magnetic resonance approach,” *Catal. Today* 216 (2013) 104–110.

[13] N. P. Ramskill, A. P. E. York, A. J. Sederman, and L. F. Gladden, “Magnetic resonance velocity imaging of gas flow in a diesel particulate filter,” *Chem. Eng. Sci.* 158 (2016) 490–499.

[14] S. P. Rigby, M. Hasan, I. Hitchcock, and R. S. Fletcher, “Detection of the delayed condensation effect and determination of its impact on the accuracy of gas adsorption pore size distributions,” *Colloids Surf. A Physicochem. Eng. Asp.* 517 (2017) 33–44.

[15] T. Hughes-Riley *et al.*, “Cryogenics free production of hyperpolarized 129Xe and 83Kr for biomedical MRI applications,” *J. Magn. Reson.* 237 (2013) 23–33.

[16] J. S. Six, T. Hughes-Riley, K. F. Stupic, G. E. Pavlovskaya, and T. Meersmann, “Pathway to Cryogen Free Production of Hyperpolarized Krypton-83 and Xenon-129,” *PLoS One* 7 (2012) 11.

[17] G. Pavlovskaya, J. Six, T. Meersman, N. Gopinathan, and S. P. Rigby, “NMR imaging of low pressure, gas-phase transport in packed beds using hyperpolarized xenon-129,” *AIChE J.* 61 (2015) 4013–4019.

[18] N. J. Rogers, F. Hill-Casey, K. F. Stupic, J. S. Six, C. Lesbats, S. P. Rigby, J. Fraissard, G. E. Pavlovskaya, and T. Meersmann, "Molecular Hydrogen and Catalytic Combustion in the Production of Hyperpolarized ^{83}Kr and ^{129}Xe MRI Contrast Agents." *Proc. Nat. Acad. Sci.* 113 (2016) 3146-3168.

[19] K. F. Stupic, J. S. Six, M. D. Olsen, G. E. Pavlovskaya, and T. Meersmann, ”Combustion resistance of the ^{129}Xe hyperpolarized nuclear spin state.”, *Phys. Chem. Chem. Phys*. 15 (2013) 94-97.

[20] P.M. Glover, B. Newling, C. Poirier, B.J. Balcom, "A novel high temperature H-1 NMR imaging probe for combustion studies: The behaviour of both a lit and unlit methane gas jet", *J. Magn Reson* 176 (2005) 79-86.

[21] D. B. Burueva, E. V. Pokochueva, X. Wang, M. Filkins, A. I. Svyatova, S. P. Rigby, C. Wang, G. E. Pavlovskaya, K. V. Kovtunov,* T. Meersmann,* and I. V. Koptyug, "In Situ Monitoring of Heretogeneous Catalytic Hydrogenation Via ^{129}Xe NMR Spectroscopy and Proton MRI", *ACS Catalysis* 10 (2020) 1417-1422.

[22] R. W. Mair, R. Wang, M. S. Rosen, D. Candela, D. G. Cory, and R. L. Walsworth, “Applications of controlled-flow laser-polarized xenon gas to porous and granular media study,” *Magn. Reson. Imaging* 21 (2003) 287–292.

[23] R. W. Mair, P. N. Sen, M. D. Hürlimann, S. Patz, D. G. Cory, and R. L. Walsworth, "The Narrow Pulse Approximation and Long Length Scale Determination in Xenon Gas Diffusion NMR Studies of Model Porous Media," *J. Magn. Reson.* 156 (2002) 202–212.

[24] R. W. Mair *et al.*, "Probing porous media with gas diffusion NMR.," *Phys. Rev. Lett.* 83 (1999) 3324–7.

[25] L. G. Kaiser, T. Meersmann, J. W. Logan, and A. Pines, "Visualization of gas flow and diffusion in porous media.," *Proc. Natl. Acad. Sci. U. S. A.* 97 (2000) 2414–2418.

[26] L. G. Kaiser, J. W. Logan, T. Meersmann, and A. Pines, "Dynamic NMR microscopy of gas phase Poiseuille flow," *J. Magn. Reson.* 149 (2001) 144–148.

[27] K. V. Kovtunov, V. V. Zhivonitko, I. V. Skovpin, D. A. Barskiy, and I. V. Koptyug, "Parahydrogen-Induced Polarization in Heterogeneous Catalytic Processes," in *TripleC* 11 (2012) 123–180.

[28] E. Harel, J. Granwehr, J. A. Seeley, and A. Pines, "Multiphase imaging of gas flow in a nanoporous material using remote-detection NMR," *Nat. Mater.* 5 (2006) 321–327.

[29] V. V. Zhivonitko, V. V. Telkki, and I. V. Koptyug, "Characterization of microfluidic gas reactors using remote-detection MRI and parahydrogen-induced polarization," *Angew. Chemie - Int. Ed.* 51 (2012) 8054–8058.

[30] J. Granwehr *et al.*, "Time-of-Flight Flow Imaging Using NMR Remote Detection," *Phys. Rev. Lett* 95 (2005) 75503.

[31] R. Mokso, C. M. Schlepütz, G. Theidel, H. Billich, E. Schmid, T. Celcer, G. Mikuljan, L. Sala, F. Marone, N. Schlumpf, M. Stampanoni. GigaFRoST: The gigabit fast readout system for tomography, Journal of Synchrotron Radiation 24 (2017) 1250-

1259.

[32] D. Haberthür, C. Hintermüller, F. Marone, J. C. Schittny, and M. Stampanoni, "Radiation dose optimized lateral expansion of the field of view in synchrotron radiation X-ray tomographic microscopy," *J. Synchrotron Rad.* 17 (2010) 590–599.

[33] D. Paganin, S. C. Mayo, T. E. Gureyev, P. R. Miller, S. W. Wilkins. Simultaneous phase and amplitude extraction from a single defocused image of a homogeneous object. Journal of Microscopy, 206 (2002) 33–40.

[34] F. Marone, and M. Stampanoni, "Regridding reconstruction algorithm for real time tomographic imaging," *J. Synchrotron Rad.* 19 (2012) 1029-1037..

[35] A. Parslow, A. Cardona, and R. J. Bryson-Richardson, "Sample drift correction following 4D confocal time-lapse imaging," *J. Vis. Exp*. 86 (2014) e51086 1-4.

[36] J. Schindelin, I. Arganda-Carreras, E. Frise, V. Kaynig, M. Longair, T. Pietzsch, S. Preibisch, C. Rueden, S. Saalfeld, B. Schmid, J. Y. Tinevez, D. J. White, V. Hartenstein, K. Eliceiri, P. Tomancak, A. Cardona. Fiji: an open-source platform for biological-image analysis, Nature methods 9 (2012) 676-682.

[37] S. P. Rigby and K. J. Edler, "The Influence of Mercury Contact Angle, Surface Tension, and Retraction Mechanism on the Interpretation of Mercury Porosimetry Data," *J. Colloid Interface Sci.* 250 (2002) 175–190.

[38] J. Kloubek, "Hysteresis in porosimetry," *Powder Technol.* 29 (1981) 63–73.

[39] K. R. Brownstein and C. E. Tarr, "Spin-lattice relaxation in a system governed by diffusion," *J. Magn. Reson.* 26 (1977) 17–24.

[40] K. R. Brownstein and C. E. Tarr, "Importance of classical diffusion in NMR studies of water in biological cells," *Phys. Rev. A* 19 (1979) 2446–2453.

[41] P. T. Callaghan, *Translational Dynamics and Magnetic Resonance: Principles of Pulsed Gradient Spin Echo NMR*. OUP Oxford, 2011.

[42] E. Brunner, “Applications of laser-polarized Xe-129 under continuous flow,” *Magn. Reson. Chem.* 37 (1999) S22.

[43] J. H. Gao, L. Lemen, J. Xiong, B. Patyal, and P. T. Fox, “Magnetization and diffusion effects in NMR imaging of hyperpolarized substances,” *Magn. Reson. Med.* 37 (1997) 153–158.Z. I.

[44] K. F. Stupic, N. D. Elkins, G. E. Pavlovskaya, J. E. Repine, and T. Meersmann, “Effects of pulmonary inhalation on hyperpolarized krypton-83 magnetic resonance T 1 relaxation,” *Phys. Med. Biol.* 56 (2011) 3731–3748.

[45] Cleveland and T. Meersmann, “Density-independent contributions to longitudinal relaxation in 83Kr,” *ChemPhysChem* 9 (2008) 1375–1379.

[46] F. Chauvet, P. Duru, S. Geoffroy, and M. Prat, “Three Periods of Drying of a Single Square Capillary Tube,” *Phys. Rev. Lett.* 103 (2009) 124502–1–124502–4.

[47] A. K. Heibel, T. W. J. Scheenen, J. J. Heiszwolf, H. Van As, F. Kapteijn, J. A. Moulijn, "Gas and liquid phase distribution and their effect on reactor performance in the monolith film flow reactor," *Chem. Engng Sci.* 56 (2001) 5935–5944.

[48] A. K. Heibel, F.J. Vergeldt, H. Van As, F. Kapteijn, J. A. Moulijn,T. Boger, " Gas and Liquid Distribution in the Monolith Film Flow Reactor.", *A.I.Ch.E.J.* 49 (2003) 3007-3017.

[49] S. Anala, G. E. Pavlovskaya, P. Pichumani, T.J. Dieken, M.D. Olsen, T. Meersmann*, “In Situ NMR of Combustion”, *J. Am. Chem. Soc*. 125 (2003) 13298 –13302